Quantifying Matrix and Fracturing Water Contributions to the Total Produced Water Based on the Water-flowback Responses

by

Zhanyuan Liu

A thesis submitted in partial fulfillment of the requirements for the degree of

Master of Science

in

Petroleum Engineering

Department of Civil & Environmental Engineering
University of Alberta

Abstract

The main goal of this thesis is to evaluate the possibility of quantifying matrix and fracturing water contributions to the total produced water based on the water-flowback responses without analyzing water chemical data. We analyze flowback production data of 380 multi-fractured horizontal oil wells completed in the Montney Formation and 90 oil and gas wells completed in the Duvernay and Horn River formations. We hypothesize that: 1) the slope of water-flowback harmonic decline (HD) profiles (m_{HD}) is proportional to the slope of rate-normalized pressure (RNP) plots (m_{RNP}), and 2) both m_{RNP} and m_{HD} are inversely proportional to the amount of water influx from matrix into fractures. To verify our hypothesis, we 1) modify the previous HD and single-phase flowing material balance models by considering the water influx from matrix into fractures, 2) classify the studied wells based on observed trends, 3) construct RNP diagnostic plots of the studied wells, 4) investigate the relationship between m_{HD} and m_{RNP}, 5) analyze log data and estimate average initial water saturation (S_{wi}) for the studied wells, and 6) investigate the relationship between of m_{HD} and S_{wi}. The results show that m_{HD} for all the studied wells ranges from 0.00001 to 0.036 $1/m^3$ with a mean value of 0.0056 $1/m^3$. Wells with higher m_{HD} have relatively higher m_{RNP} values. In contrast, wells with very low m_{HD} show no significant decline in water rate through the entire flowback process and relatively low or inconsistent m_{RNP} values on the corresponding plots of RNP versus material balance time (MBT). We also observe a negative correlation between m_{HD} and S_{wi} obtained by analysis of wireline log data. This correlation and the positive correlation between m_{HD} and m_{RNP} indicate that as S_{wi} increases, water influx from matrix to fracture increases, and thus, both m_{HD} and m_{RNP} decrease. Based on our modified models and the observed correlations, we develop a method to approximately differentiate between matrix and fracturing water. The applications of our heuristic method on field data shows 1) fracturing water production dominates

the total water recovery for wells with higher m_{RNP}, and 2) matrix water production dominates the total water recovery for wells with lower m_{RNP}.

Preface

This thesis is original work by zhanyuan Liu. Some parts of this research in chapter 1, 2 and 3 of this thesis have been published or presented as:

- Liu, Zhanyuan, Moussa, Tamer, and Hassan Dehghanpour. "Flowback Pattern-Recognition to Distinguish Between Formation and Fracturing Water Recovery." Paper presented at the SPE Canadian Energy Technology Conference, Calgary, Alberta, Canada, March 2022.

Dedication

To my dearest parents,

Mr. Haitao Liu, and Mrs. Dongxia Huang.

Acknowledgements

I feel grateful to my supervisor Dr. Hassan Dehghanpour for his patient and insightful guidance, kind support, continuous encouragement throughout my master study. My master study and research would not have been finished without his guidance. He inspired me a lot during the past two years and his teachings will be with me through my life and future career.

I would like to extend my appreciation to all the people who helped me. My special thanks to Dr. Tamer Moussa for his patient, valuable suggestions and comments on my master research. This study would not have been completed without his help.

I would also like to acknowledge the Natural Sciences and Engineering Research Council of Canada (NSERC) and geoLOGIC for supporting my study.

Finally, I would also like to express my appreciation from my bottom of my heart to my parents Mr.Haitao Liu Yuan and Mrs. Dongxia Huang for their moral support and continuous encouragement. Their love and moral support are key factors to help me to complete my research study.

Table of Contents

Abstract ... ii
Preface ... iv
Dedication ... v
Acknowledgements ... vi
List of Tables ... ix
List of Figures ... x
Nomenclature ... xii
Abbreviations ... xiv
Chapter 1:Introduction ... 1
1.1 Background ... 1
1.2 Objective of Research ... 3
1.3 Structure of Thesis ... 4
Chapter 2: Literature Review ... 6
2.1 Review of Montney, Duvernay and Horn River Formations ... 6
2.1.1 Montney Formation ... 6
2.1.2 Duvernay Formation ... 7
2.1.3 Horn River Formation ... 8
2.2 Previous Studies on Chemical Analysis of Flowback Water ... 9
2.3 Previous Studies on RNP Diagnostic Plot ... 11
Chapter 3: Well Statistics and Wireline Log Data ... 15
3.1 Introduction ... 15
3.2 Well statistics ... 15
3.3 Wireline log data ... 16
3.3.1 Fracture stages ... 16
3.3.2 Gamma-ray log ... 17
3.3.3 Porosity and resistivity logs ... 17
3.4 Frequency distributions of m_{HD}, m_{RNP}, and S_{wi} ... 18
Chapter 4: Results of Case Studies 1 and 2 ... 20
4.1 Introduction ... 20
4.2 Results of case study 1: Oil wells completed in the Montney Formation ... 20
4.2.1 Overview of water-flowback HD profile ... 20
4.2.2 Comparing RNP plots of the wells with high and low m_{HD} ... 22
4.2.3 Correlation between m_{HD} and m_{RNP} ... 23
4.2.4 S_{wi} estimation by using well-log data ... 25
4.2.5 Correlation between m_{HD} and S_{wi} ... 26

4.3 Results of case study 2: Oil and gas wells from Horn River and Duvernay Formations ... 28
4.3.1 Correlation between m_{HD} and m_{RNP} ... 29
4.3.2 Correlation between m_{HD} and S_{wi} ... 30
4.4 Estimating fracturing and formation water production during water-flowback process ... 31
4.4.1 Analysis procedure of the heuristic model ... 31
4.4.2 Example applications ... 33
Chapter 5: Theoretical analysis and Heuristic Model for Estimating Formation and Fracturing Water Contributions during Water-flowback Processes ... 35
5.1 Introduction ... 35
5.2 Pseudo steady-state (PSS) solution of water RNP diagnostic plot ... 35
5.4 Uncertainties and limitations ... 47
5.4.1 Heuristic model ... 47
5.4.2 Estimation of S_{wi} ... 48
Chapter 6: Conclusions and Recommendations for Future Study ... 51
6.1 Conclusions ... 51
6.2 Recommendations for Future Study ... 52
Bibliography ... 54
Appendix A ... 58
Appendix B ... 59

List of Tables

Table 3.1: General statistics for the studied wells in case studies 1 and 2 15

Table 3.2: Fracture stages information of a sample Montney well..... 16

Table 3.3: Gamma-ray log data of a sample Montney well..... 17

Table 3.4: Measured depth versus a) porosity, and b) resistivity log data for the studied well.... 18

Table 4.1: Key completion parameters for 25 oil wells from the Montney Formation 28

Table 4.2: Calculated values for $Qwma$ and Qwf at the end of the flowback process for the sample oil well 34

Table 5.1: Assumed values of each parameter in m_{RNPwf} model 40

Table 5.2: Assumed values of each parameter in m_{RNP} model 42

Table 5.3: Assumed values of each parameter in transient model..... 46

Table 5.4: Error analysis of ρa for calculating S_{wi} for the Montney, Duvernay, and Horn River wells 49

Table 5.5: The calculated error range for calculating S_{wi} for the Duvernay and Horn River formations 50

Table B-1: Calculated values for $Qwma$ and Qwf at the end of the flowback process for the sample oil well A 59

Table B-2: Calculated values for $Qwma$ and Qwf at the end of the flowback process for the sample oil well B 60

Table B-3: Calculated values for $Qwma$ and Qwf at the end of the flowback process for the sample oil well C 61

List of Figures

Figure 2.1: Location of Montney Formation and stratigraphy (Moslow et al. 1997) 6

Figure 2.2: Location of Duvernay Formation and lithology (Pengwei Wang et al. 2016) 7

Figure 2.3: Location of Horn River Formation 8

Figure 2.4:Log-Log plot of water/oil rate-normalized pressure (RNP) before jet-pump installation for Well 2 (Moussa et al. 2020) 14

Figure 3.1: Frequency distributions of a) m_{HD}, b) m_{RNP}, and c) S_{wi} for the studied wells with both pressure and log data. 19

Figure 4.1: Semi-log plots of qw and qo versus Qw for three sample oil wells with: a) high m_{HD}, b) low m_{HD}, and c) early increasing trend of qw due to frequent choke size variations 22

Figure 4.2:Log-log plots of RNP versus MBT for sample oil wells with lower m_{HD}. 22

Figure 4.3: Log-log plots of RNP versus MBT for sample oil wells with higher m_{HD} 23

The starting points of red curves indicate the starting points of consistent linear trends on the RNP plots. 23

Figure 4.4: m_{HD} versus m_{RNP} for 127 Montney wells on a) cartesian plot and b) semi-log plot .. 24

Figure 4.5: m_{HD} versus S_{wi} for 100 Montney wells 27

Figure 4.6: a) m_{HD} and b) water load recovery versus S_{wi} for 25 Montney wells with similar completion parameters 28

Figure 4.7: m_{HD} versus m_{RNP} on a) cartesian plot and b) semi-log plot for the 216 studied wells 29

Figure 4.8: m_{HD} versus S_{wi} on a) cartesian plot and b) semi-log plot for the 189 studied wells .. 30

Figure 4.9: RNP versus MBT for a sample oil well on a) log-log plot and b) cartesian plot 34

Figure 4.10: Semi-log plots of calculated qw, qwf, and $qwma$ versus Qw for a sample oil well 34

Figure 5.1: 2-D view of a fractured horizontal well. The black arrows show the flow direction of water in fractures and in stimulated matrix. The red lines represent no-flow boundaries of stimulated matrix. 35

Figure 5.2: Effects of increasing VR on a) cartesian plot, and b) log-log plot of RNP_{wf} versus MBT. 41

Figure 5.3: Effects of increasing VR on a) cartesian plot, and b) log-log plot of RNP versus MBT. 43

Figure 5.4: 2-D view of a fractured horizontal well in TS model..... 43

Figure 5.5: Effects of increasing $Swma$ on a) cartesian plot, and b) log-log plot of RNP versus t. 46

Figure A-1: Measured depth versus Gamma ray for sample oil well. Linear shale index is used as the value of *Vsh* in the Simandoux equation..... 58

Figure B-1: RNP versus MBT for sample oil well A on a) log-log plot and b) cartesian plots .. 59

Figure B-2: Semi-log plots of qw, qwf, and $qwma$ versus Qw for a sample oil well A 59

Figure B-3: RNP versus MBT for sample oil well B on a) log-log plot and b) cartesian plots... 60

Figure B-4: Semi-log plots of qw, qwf, and $qwma$ versus Qw for a sample oil well B 60

Figure B-5: RNP versus MBT for sample oil well C on a) log-log plot and b) cartesian plots... 61

Figure B-6: Semi-log plots of qw, qwf, and $qwma$ versus Qw for a sample oil well C 61

Nomenclature

q_w Water rate, m^3/day

q_{wma} Formation water rate, m^3/day

q_{wf} Fracturing water rate, m^3/day

q_o Oil rate, m^3/day

Q_w Cumulative water production, m^3

Q_{wma} Cumulative formation water production, m^3

Q_{wf} Cumulative fracturing water production, m^3

Q_o Cumulative oil production, m^3

D_i Initial water decline rate, $1/day$

P_c Casing pressure, $kpaa$

P_{wf} Well bottom hole flowing pressure, $kpaa$

P_{fi} Initial fracture pressure, $kpaa$

P_f Fracture pressure, $kpaa$

P_{ma} Matrix pressure, $kpaa$

S_{wi} Initial water saturation, $fraction$

a Tortuosity

m Cementation component

n Saturation exponent

R_w Water resistivity, $m\Omega$

R_t True resistivity, $m\Omega$

V_{sh} Shale volume, *fraction*

R_{sh} Shale resistivity, $m\Omega$

ρ_a Assumed matrix density, *g/cc*

ρ_t True matrix density, *g/cc*

ρ_{wb} Average density of water that recovered in the wellbore, *g/cc*

ρ_{wma} Average density of water that recovered in the matrix, *g/cc*

ρ_f Average density of total flowback water, *g/cc*

V_f Fracture volume, m^3

V_{wb} Wellbore volume, m^3

C_f Total compressibility in the fractures, psi^{-1}

C_{ma} Total compressibility in the matrix, psi^{-1}

$\emptyset_f$ Fracture porosity, *fraction*

$\emptyset_{ma}$ Matrix porosity, *fraction*

K_f Fracture permeability, *md*

K_{ma} Matrix permeability, *md*

μ Water viscosity, *cp*

Abbreviations

FB Flowback

HD Harmonic decline

RNP Rate normalized pressure, $kpaa \cdot day/m^3$

MBT Material balance time, day

LR Load recovery, $fraction$

TIV Total injection volume, m^3

TVD True vertical depth, m

Chapter 1:Introduction

1.1 Background

Although there are strict regulations for disposal and re-use of produced water, regulating the flowback operations and reporting the corresponding data have been challenging (Gregory et al. 2011). For example, it is hard for the industry to quantify matrix and fracturing water contributions to the total produced water for reservoirs with high water cut and initial pressure.

Flowback chemical analysis has been considered as a complementary approach for evaluating fracturing operations and characterizing reservoir properties. Examples of recent studies include those by Gdanski et al. (2007), Warner et al. (2014), Zolfaghari et al. (2015) and Imma et al. (2015). Gdanski et al. (2007) analyzed the ionic composition of the flowback-water samples and developed a new model that embodies the physics of flow during back-production of water after fracturing operations. Their model shows the difference between the composition of formation and fracturing water. Warner et al. (2014) investigated the geochemical fingerprints of produced flowback water after high-volume hydraulic fracturing of unconventional oil and gas wells completed in the Marcellus and Fayetteville shale formations. They investigated the variations of inorganic chemicals in produced fluid and proposed a specific tracer to differentiate the formation and fracturing water based on chemical elements of produced water. Zolfaghari et al (2015) investigated the source of produced flowback salts and the mechanisms controlling the flowback water chemistry. In their study, samples of flowback water and downhole shales were analyzed to investigate shale-water interactions. To evaluate chemical components in the produced flowback water, Imma et al (2015) presented and discussed multiple analytical techniques including 1) organic/inorganic analysis, and 2) gas/liquid chromatography–mass spectrometry. These methods

could be potentially used for detection of the natural components from a geological formation and chemical additives in flowback and produced water.

The previous techniques can be used to distinguish between produced fracturing and formation water based on the chemical analysis. However, they are expensive and time- consuming processes since they require analyzing reservoir rock properties and chemical composition of produced water samples that are not always available. Therefore, the objective of this research is to evaluate the possibility of distinguishing between fracturing and formation water by volumetric and pressure analysis of produced water when chemical data are unavailable.

The diagnostic plot of RNP versus MBT has been adopted to be used for analyzing flow regimes during water flowback processes. A unit-slope on the RNP plot represents the pseudo-steady-state flow regime of water flowback (Abbasi et al. 2014, Ezulike et al. 2016) and indicates negligible water influx from matrix into fractures (Fu et al. 2017, Sabbir et al. 2019). For example, wells may have "pressure-supercharge" effect (initial fracture pressure is much higher than matrix pressure) during early flowback process. However, a half slope on the RNP plot represents transient linear flow behaviour and suggests fluid influx from matrix blocks into fractures (Bello et al. 2009, Song and Ehlig-Economides. 2011). In addition, recent studies (Moussa et al. 2020) show that oil breakthrough has insignificant effects on water flow regime analysis since oil and water tend to flow independently through their own network. Therefore, we hypothesize that m_{RNP} on the water RNP plot is inversely proportional to the amount of matrix water influx for the studied oil wells.

Fu et al. (2018) observed HD trends on the semi-log plots of water-flowback rate (q_w) versus cumulative water production (Q_w) during two-phase flowback. Based on HD model (Lee and Wattenbarger 1996), we hypothesize that m_{HD} is inversely proportional to the amount of formation water influx. Therefore, we test the following hypotheses in our study: 1) m_{HD} positively correlates

with m_{RNP}, and 2) both m_{RNP} and m_{HD} values are inversely correlated with the amount of matrix water influx from matrix into fractures.

Formation water mobility depends on initial water saturation (S_{wi}) and also irreducible water saturation of the reservoir rock. There are two common methods that can be used to approximately estimate S_{wi} using resistivity and porosity logs if core analysis data are unavailable. The water saturation model proposed by Archie (1952) usually works well for non-conductive rock matrix (such as clean sandstone), and it overestimates water saturation of rock formations with clay minerals. Later, Simandoux (1963) analyzed "homogeneous mixtures of sorted sand and natural clay in various proportions" and proposed a model to consider excess electrical conductivity caused by clay minerals in the rock matrix.

In this thesis, we first present the workflow for testing our hypotheses by using two case studies. Then, we discuss the results from the analysis of the wells completed in the Montney, Duvernay, and Horn River Formations. Next, we develop a mathematical model based on the observed diagnostic trends to quantify matrix and fracturing water contributions to the total produced water. Next, we extend the single-phase flowback model (Abbasi et al. 2014) by considering the water influx from matrix into fractures for verifying the proposed hypotheses and the feasibility of our heuristic model. Finally, we discuss the limitations and uncertainties of the proposed method.

1.2 Objective and Methodology of Research

The main objective of this thesis is to quantify matrix and fracturing water contributions to the total produced water based on the water flowback response. To verify our hypothesises, we proposed the approach consists of the following steps:

1) Extract flowback data of the studied wells.

2) Construct semi-log plots of q_w versus Q_w for studied wells. Then, ignore the early noisy data and estimate m_{HD}.

3) Construct diagnostic plots of RNP versus MBT for the studied wells and estimate m_{RNP}.

4) Investigate the relationship between m_{RNP} and the m_{HD}.

5) Collect and analyze the available well log data including 1) neutron porosity, 2) deep resistivity and 3) gamma-ray log.

6) Estimate the average S_{wi} for the studied wells by using the equation proposed by Simandoux (1963).

7) Investigate the effects of S_{wi} on m_{HD}, assuming S_{wi} is proportional to the formation water mobility.

8) Conduct theoretical analysis by extending previously proposed RNP and HD models.

9) Propose a new heuristic model to approximately quantify matrix and fracturing water contributions to the total produced water during water-flowback processes.

1.3 Structure of Thesis

Chapter 1 briefly introduces the research background, research gap and objectives of this study.

Chapter 2 reviews previous studies and proposed techniques which can be used to distinguish between fracturing water and formation water based on water chemical analysis.

Chapter 3 shows the general statistics and wireline log data for the studied oil wells.

Chapter 4 tests our hypothesises and presents the results of studied oil wells from the Montney, Horn River, and Duvernay Formations. Then, we propose the heuristic model to approximately quantify matrix and fracturing water contributions to the total produced water during flowback processes.

Chapter 5 present the theoretical analysis to further verify the hypothesises of this study and the feasibility of our heuristic model.

Chapter 6 summarizes the main findings and conclusions of this study. The recommendations for future studies are also presented in this chapter.

Chapter 2: Literature Review

2.1 Review of Montney, Duvernay and Horn River Formations

In this section, we briefly review the stratigraphy, lithology, and oil/gas reserves in the studied formations.

2.1.1 Montney Formation

The Montney Formation is a stratigraphical unit of Lower Triassic age in British Columbia and Alberta, as shown in **Figure 2.1.** It covers approximately 130,000 km^2 (NEB et al. 2013) and has been the major target of tight oil and shale gas exploration. The Lower Montney is mainly composed of dark grey shales and dolomitic siltstone while the Upper Montney contains light brown siltstone interlaminated with fine grained sandstone.

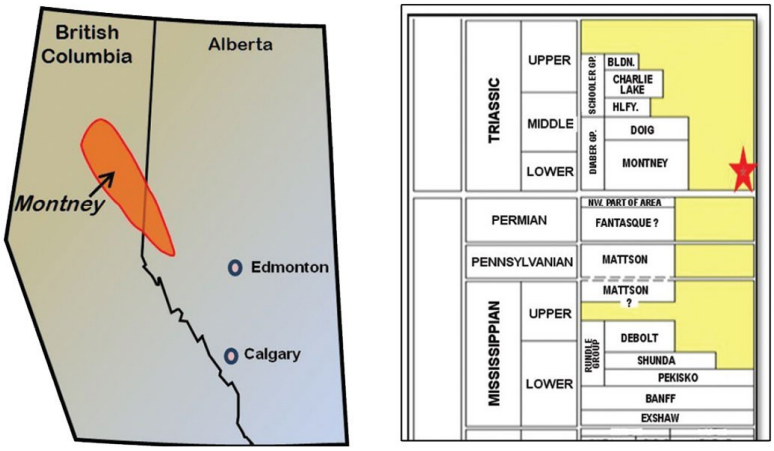

Figure 2.1: Location of Montney Formation and stratigraphy (Moslow et al. 1997)

The ultimate potential for in the Montney Formation is estimated to be very large, with expected marketable natural gas volumes of 12,719 billion m^3, natural gas liquid (NGL) volumes of 2,308 million m^3 , and oil volumes of 179 million m^3 (NEB et al. 2013).

2.1.2 Duvernay Formation

The Duvernay Formation locates over central Alberta and the sediments were deposited in a marine basin on the bottom of the seafloor surrounding the Leduc Formation reefs, as shown in **Figure 2.2** Also, it contains two geological plays, which are West Shale Basin and East Shale Basin.

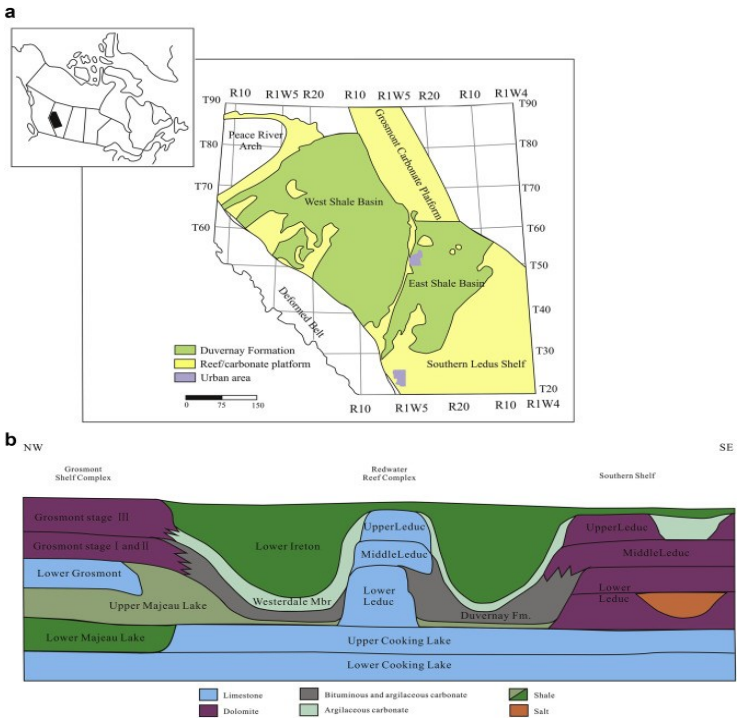

Figure 2.2: Location of Duvernay Formation and lithology (Pengwei Wang et al. 2016)

The lithology of the Duvernay Formation includes shale and limestone. The West Shale Basin has higher proportion of shale while East Shale Basin has higher proportion of limestone. The formation thickness ranges from 1 to 105 m across the depositional extent, and depth ranges from 850 m to 5400 m from northeast to southwest. According to Alberta Energy Regulator (ARE) published resource (Rokosh et al. 2012), the total in-place resource contains 350 to 540 trillion ft^3 of natural gas, 7 to 16 billion bbl of natural gas liquids, and 44 to 81 billion bbl of oil, respectively.

2.1.3 Horn River Formation

The Horn River Formation is a stratigraphic unit of Devonian age in northeastern British Columbia and extends to Great Slave Lake in the Northwest Territories, as shown in **Figure 2.3** Also, it has a maximum thickness of 320 m in the subsurface of the Fort Nelson area. The Horn River Formation sediments are mainly dark siliceous shale, and bituminous limestone (Mossop et al. 1994).

Figure 2.3: Location of Horn River Formation

The shale gas resource is the major target in the Horn River Formation. The original-gas-in-place volumes are approximately estimated as 500 trillion ft^3 , making it the third largest North American natural gas accumulation discovered prior to 2010 (Simon Mauger et al. 2011).

2.2 Previous Studies on Chemical Analysis of Flowback Water

Flowback chemical analysis has been considered as a complementary approach for evaluating fracturing operations and characterizing reservoir properties. In this section, we briefly review the previous studies on chemical analysis of flowback water.

Gdanski et al. (2007) analyzed the ionic composition of the flowback-water samples and developed a new model that embodies the physics of flow during back-production of water after fracturing treatment. The authors proposed a two-step process to analyze the water chemical movement. The first step was to obtain the pressure solution for physical movement of the water. The second step was to analyze the chemical movement of the water. The mass balance equation of chemicals in the grid block was given by:

$$(Ci,jVi,j)^{n+1}=(Ci,jVi,j)^{n}-(Ci,j\Delta Vi\pm1,j\pm1)^{n+1}+(Ci\pm1,j\pm1\Delta Vi\pm1,j\pm1)^{n+1} \quad (2.1)$$

Here, C is concentration and has unit of moles/L. This equation represents that the chemical concentration in a grid block at time step n+1 is equal to the original chemical concertation minus the amount of that exits from the block, and plus the amount of that flow into the block. The volume changes were estimated from flow equation and pressure solution at time step n+1 gives:

$$\frac{\Delta V}{\Delta t} = q = \frac{k_w A}{\mu_w}\frac{\Delta P_w}{\Delta L} \quad (2.2)$$

Here, ΔV is the flow volume; Δt is the time step; q is the water flow rate; ΔP_w is the pressure drop in the water phase; k_w is the water relative permeability; μ_w is the water viscosity; A is the area of grid block; ΔL is the distance between two blocks. This model is useful to distinguish between formation and fracturing water recovery since it considered formation water having different ionic compositions from the fracturing fluid. Matching the compositions requires: 1) proper matching of the water production during water-flowback process, 2) proper estimation of relative permeabilities and capillary pressures, and 3) reasonable estimation of amount of effective

fractures. The figures below were the stimulation results for a sample gas well in their study. **Figure 2.4a** shows fractional composition of fluid type versus cumulative water production while **Figure 2.4b** shows the potassium (K), sodium (Na), and chloride (CL) return profiles for this sample stimulation. In their study, the tubing displacement and fracturing fluid were composed of 3.7% (weight percentage) and 6.5% KCL, respectively. The formation brine was composed of 2.9% NaCL. Although the tubing displacement and fracturing fluid were based on KCL, the difference in their chemical compositions can makes the identification obvious. Therefore, the similarities in the patterns were noticeable between **Figure 2.4a** and **2.4b**.

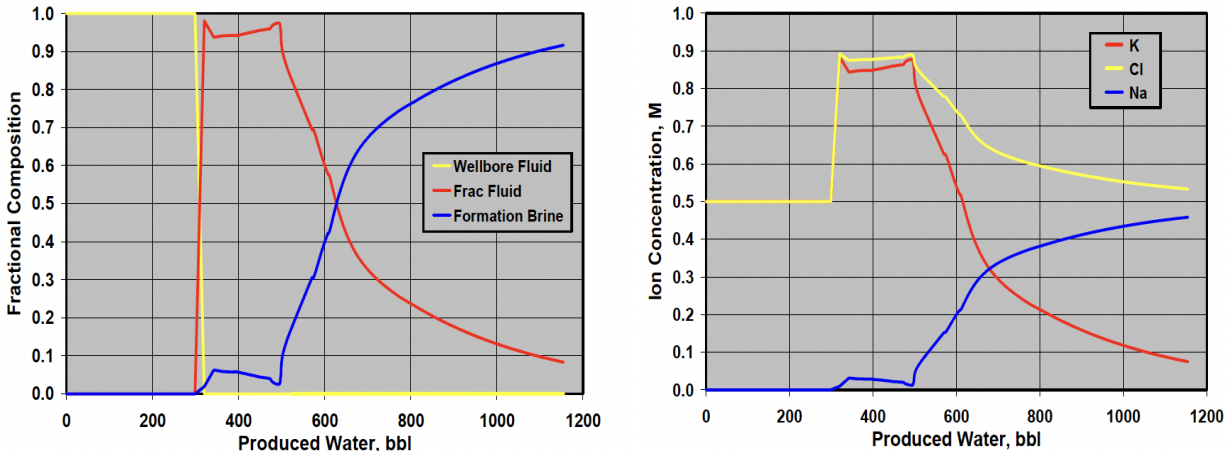

(a) (b)

Figure 2.4:a) Fluid identification and b) chemical production for a sample gas well (Gdanski et al. 2007)

Warner et al. (2014) investigated the geochemical fingerprints of produced flowback fluids after high-volume hydraulic fracturing of unconventional oil and gas wells completed in the Marcellus and Fayetteville black shale formations. They investigated the variations of inorganic chemicals in fracturing fluid and proposed a specific tracer to differentiate the formation water and fracturing water based on chemical elements of produced water.

Zolfaghari et al (2015) investigated the source of flowback salts and the mechanisms controlling the produced water chemistry**.** In their study, samples of flowback water and downhole shales from the Muskwa, Otter-Park, and Evie members of the Horn River Basin were analyzed to investigate the water-shale interactions. Form their observations, the salts concentration and electric conductivity in the water samples are generally increase with respect to flowback time. The concentrations of Na^+, K^+, Ca^{2+}, and Ba^{2+} are also increase over flowback time.

To evaluate chemical components in the produced flowback fluid, Imma et al (2015) presented and discussed multiple analytical techniques, involving: 1) organic/inorganic analysis, and 2) gas/liquid chromatography–mass spectrometry. These methods could be potentially used for detection of the natural components from a geological formation and chemical additives in flowback and produced water.

Overall, the chemical compositions of produced water are highly depend on the well-completion data and rock properties of the studied formations. Therefore, the previous studies on chemical analysis of flowback water are helpful to distinguish between formation and fracturing water recovery when actual field data and water chemical data are available.

2.3 Previous Studies on RNP Diagnostic Plot

Although the proposed flowback chemical analysis can be utilized to distinguish between fracturing fluid and formation water, they are still commercially expensive and time- consuming processes for the industry to report load-fluid recovery. In this section, we review the previous studies on the diagnostic plot of RNP versus MBT, which gives us ideas on formation water mobility.

Abbasi et al (2014) proposed radial tank model based on the diffusivity equation for single-phase water flow through the hydraulic fractures towards the horizontal well during early flowback period. The proposed model can be utilized to evaluate wellbore and fracture properties:

$$\frac{P_i - P_{wf}}{q_s} = \frac{N_p B}{q_s C_{st}} + \frac{\emptyset_f C_t \mu B}{2 C_{st} K_f} r_e^2 \left[\frac{1}{2} \ln\left(\frac{4A}{C_A \gamma r_w^2}\right)\right] \quad (2.3)$$

Where P_i is initial fracture pressure. P_{wf} is well bottom hole flowing pressure. q_s and N_p represent surface flowrate and cumulative production of fracturing water. B is formation volume factor. C_{st} represents total storage coefficient. $P_i - P_{wf}/q_s$ and N_p/q_s are referred as RNP and MBT. The second term on the right-hand side accounts for well geometry and fracture properties. For this model, the authors assumed only fracturing water will be produced during very early time of flowback processes. They also observed the proposed linear relationship between RNP and MBT for 3 studied wells completed in tight oil and gas reservoirs.

Ezulike et al (2016) used data-driven approach to observe changes in the fluid-flow mechanisms of multistage-fractured wells and proposed a two-phase flowback model based on their observations. All of the 15 studied wells completed in the Muskwa, Otter Park, and Woodford formations show nearly unit slopes on RNP diagnostic plots during early flowback period. They suggested that the observed unit-slope on the RNP plot represents the pseudo-steady-state (PSS) flow regime of water flowback and indicates negligible fluid influx from matrix into fractures. PSS of water flow can be explained by the "pressure-supercharge" effect: During early time, the average pressure in the matrix is still much larger than that in the fractures. However, the well bottomhole flowing pressure is less than both matrix and fracture pressure, thus, fluid can flow to the surface without additional support by fluid influx from the matrix. During late flowback period, the studied wells show transient flow regime of water-flowback and indicates the average pressure

in the fractures is less than that in the matrix. Therefore, there is fluid influx from the matrix into the fractures.

Bello et al (2009) analyzed fractured shale gas horizontal wells in the Barnett shale. The fractured shale gas reservoir system was described as a linear dual porosity model and all the studied wells exhibited transient linear behavior: one-half slope on the log-log plot of RNP against time. The transient linear flow regime indicates drainage of fluid from low permeability matrix into adjacent fractures.

The diagnostic plot of RNP versus MBT has been adopted to be used for analyzing the flow regimes during water-flowback processes. Moussa et al (2020) analyzed multiphase production data of six multi-fractured horizontal black-oil wells completed in the Eagleford Formation. **Figure 2.5** shows RNP_o and RNP_w under bottomhole conditions for one of six wells in their study. The plot of RNP_w shows a unit slope during early production time, indicating boundary dominated flow of water. However, the plot of RNP_o shows steady state flow of oil phase and there is oil influx from matrix into fractures. The authors observed similar results for the other studied wells and all the wells show there is no significant changes in the slope of RNP_w after the oil breakthrough.

The authors suggested that oil breakthrough has insignificant effects on water flow regime analysis and oil tends to flow independently through its own network. Also, the pressure support from oil influx will be compensated by the decrease in water relative permeability due to the decrease of water saturation in the fractures. However, for a saturated oil reservoir, the gas expansion can drag the water flow through hydraulic fractures towards the wellbore. Therefore, the gas expansion increases the water-flowback rate and lead a downward deviation from a unit slope on log-log water RNP plot.

At the end of this study, we proposed a heuristic method based on the water RNP diagnostic plots to approximately quantify matrix and fracturing water contributions to the total produced water during water-flowback processes.

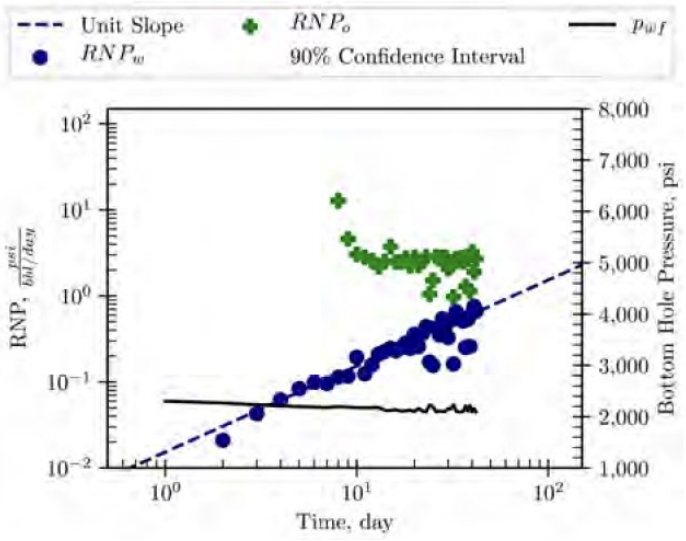

Figure 2.5:Log-Log plot of water/oil rate-normalized pressure (RNP) before jet-pump installation for Well 2 (Moussa et al. 2020)

Chapter 3: Well Statistics and Wireline Log Data

3.1 Introduction

In this study, we conduct quantitative analysis for the studied wells. This chapter presents 1) well statistics, 2) sample wireline log data which are needed in the S_{wi} estimation, and 3) frequency distributions of m_{HD}, m_{RNP}, and S_{wi} for the studied wells.

3.2 Well statistics

In this study, we first extract field data of 468 oil and gas wells completed in the Montney, Duvernay, and Horn River formations using the 'GEOscout' software. Then, we use well flowback data to construct HD profiles and RNP diagnostic plots and use wireline log data to estimate S_{wi}. **Table 3.1** lists the number of wells with pressure and log data in case studies 1 and 2. Out of 379 Montney wells in case study 1, 127 and 100 wells have available pressure and log data, respectively. In case study 2, all the studied wells from the Horn River and Duvernay formations have both pressure and log data.

Table 3.1: General statistics for the studied wells in case studies 1 and 2

	Case study 1	Case study 2	
Formation name	Montney	Horn River	Duvernay
Hydrocarbon type	Oil	Oil and gas	Oil
Number of total studied wells	379	40 (14 oil wells and 26 gas wells)	49
Number of wells with available pressure data	127	40	49
Number of wells with available log data	100	40	49
Number of fracture stages	20-42	20-31	16-33
Flowback duration, day	8-25	12-30	12-25

TVD, m	1700-3200	1800-3000	1800-3000
TIV, m^3	8000-27000	8000-12000	8000-13000
Choke size, in	38-50	40-45	37-44

3.3 Wireline log data

In this section, we present fracture stages information and wireline log data of a sample oil well completed in the Montney Formation. The wireline log data are extracted from 1) gamma-ray , 2) porosity, and 3) resistivity logs.

3.3.1 Fracture stages

Table 3.2 shows the fracture stage details of a sample oil well. In this case, the well has 24 fracture stages. The measured depth of bottom of the first stage is 4304m, and that of top of the last stage is 2245m. Therefore, we need to extract the corresponding log data within 2245 to 4304m interval of measured depth for estimating S_{wi}.

Table 3.2: Fracture stages information of a sample Montney well

Stage - Stage Number	Stage - Top Depth (m)	Stage - Bottom Depth (m)	Stage - TVD (m)
1	4277	4304	2179.6
1	4277	4304	2179.6
2	4193	4250	2180.95
3	4109	4166	2181.18
4	4025	4082	2180.2
5	3941	3998	2178.88
6	3857	3914	2180.63
7	3773	3830	2180.15
8	3689	3746	2180.98
9	3605	3662	2180.18
10	3521	3578	2179.78
11	3437	3494	2182.22
12	3353	3410	2183.06
13	3269	3326	2182.69
14	3185	3242	2183.01
15	3101	3158	2182.16
16	3017	3074	2180.63
17	2933	2990	2180.69
18	2849	2906	2181.46
18	2849	2906	2181.46
19	2765	2822	2181.27
20	2681	2738	2180.22
21	2597	2654	2180.47
22	2513	2570	2182
23	2429	2486	2181.26
24	2245	2395	2181.63

3.3.2 Gamma-ray log

Table 3.3 shows the part of measured depth versus corresponding gamma-ray values of the studied well. In this study, gamma-ray logs are used to estimate $S_{wi.}$ We observe that the log data below 2216m are unavailable for the sample well. Therefore, we use the gamma-ray value (in red color) close to the measured depth of the last fracture stage to estimate S_{wi}.

Table 3.3: Gamma-ray log data of a sample Montney well

DEPT(m)	GRGM(GAPI)
2213.5	112.7
2213.6	112.3
2213.7	110.5
2213.8	111
2213.9	111.9
2214	114.8
2214.1	115.6
2214.2	116.8
2214.3	116.6
2214.4	117.2
2214.5	117.1
2214.6	117.1
2214.7	118.1
2214.8	117.9
2214.9	118.1
2215	117.5
2215.1	118.1
2215.2	118.2
2215.3	118
2215.4	118
2215.5	117.7
2215.6	118.1
2215.7	116.8
2215.8	116.1
2215.9	114.6
2216	114.7

3.3.3 Porosity and resistivity logs

Table 3.4 shows the measured depth versus corresponding porosity and resistivity values. In this study, density-porosity (DPRS) and deep resistivity (R60O) logs are used to obtain the porosity of rock matrix and approximate formation water resistivity, respectively. Similar to gamma-ray log,

the data below 2216m are unavailable, and thus, the values close to the measured depth of the last fracture stage are used for S_{wi} estimation. More details of S_{wi} estimation are shown in the next chapter.

Table 3.4: Measured depth versus a) porosity, and b) resistivity log data for the studied well

DEPT	NPRS	DPRS
M	PERC	PERC
2213.1	15.3	1
2213.2	15.5	1.3
2213.3	15.6	1.8
2213.4	15.7	2.6
2213.5	15.7	3
2213.6	15.6	3.6
2213.7	15.6	3.5
2213.8	15.4	3.5
2213.9	15.3	3
2214	15.2	2.8
2214.1	15.2	2.5
2214.2	15.4	2.4
2214.3	15.7	2.4
2214.4	16.1	2.6
2214.5	16.3	3.1
2214.6	16.2	3.7
2214.7	16	4.1
2214.8	15.6	4.2
2214.9	15.3	4.2
2215	15.1	4
2215.1	15	3.7
2215.2	15	3.9
2215.3	14.9	4.4
2215.4	14.9	4.7
2215.5	15	4.9
2215.6	15.2	5.2
2215.7	15.3	5.4
2215.8	15.4	5.6
2215.9	15.5	6.1
2216	15.5	6.5

(a)

DEPT	R20O	R40O	R60O
M	OHMM	OHMM	OHMM
2213.5	186.7	273.6	251
2213.6	148.3	220.1	202.5
2213.7	90.8	135.7	125.3
2213.8	48.2	72.2	67
2213.9	44.6	66.6	62.2
2214	59.3	89.8	84.1
2214.1	104.8	159.2	149.7
2214.2	209.7	314.8	298.2
2214.3	230	349.5	331.9
2214.4	142.6	216.3	206.4
2214.5	77.2	116.5	111.7
2214.6	53.3	81	77.9
2214.7	40.3	60.7	58.7
2214.8	44.1	66.6	64.6
2214.9	97.8	147.9	143.9
2215	136.2	206.1	201.1
2215.1	126.6	190.1	186.2
2215.2	57.3	85.4	83.9
2215.3	50.2	76.4	75.1
2215.4	45.7	67.6	66.7
2215.5	63.7	94.9	93.8
2215.6	80	122	120.6
2215.7	36.7	54.4	53.8
2215.8	32.3	48.1	47.7
2215.9	48.6	74.3	73.5
2216	43.2	64.3	63.6

(b)

3.4 Frequency distributions of m_{HD}, m_{RNP}, and S_{wi}

In this study, we extract the water-flowback and log data of the studied wells using the 'GEOscout' software to estimate the values of m_{HD}, m_{RNP}, and S_{wi}, and conduct the statistical analysis on 'Excel spreadsheet'. **Figure 3.1** shows the frequency distribution of m_{HD}, m_{RNP}, and S_{wi} for the studied

wells. From the analysis of the data, we observe that 1) m_{HD} ranges from 0.00001 to 0.036 $1/m^3$ with a mean value of 0.0056 $1/m^3$, 2) m_{RNP} (log-log slope) ranges from 0.2 to 1 with a mean value of 0.67, and 3) S_{wi} ranges from 0.05 to 0.75 with a mean value of 0.246. We also observe that both calculated values of m_{HD} and S_{wi} follow right-skewed distributions, as shown in **Figure 3.1a** and **3.1c**, respectively. However, the calculated values of m_{RNP} follows a left-skewed distribution, as shown in **Figure 3.1b**. The correlations between 1) m_{RNP} and m_{HD}, and 2) m_{HD} and S_{wi} for wells in the two case studies are presented in the next chapter.

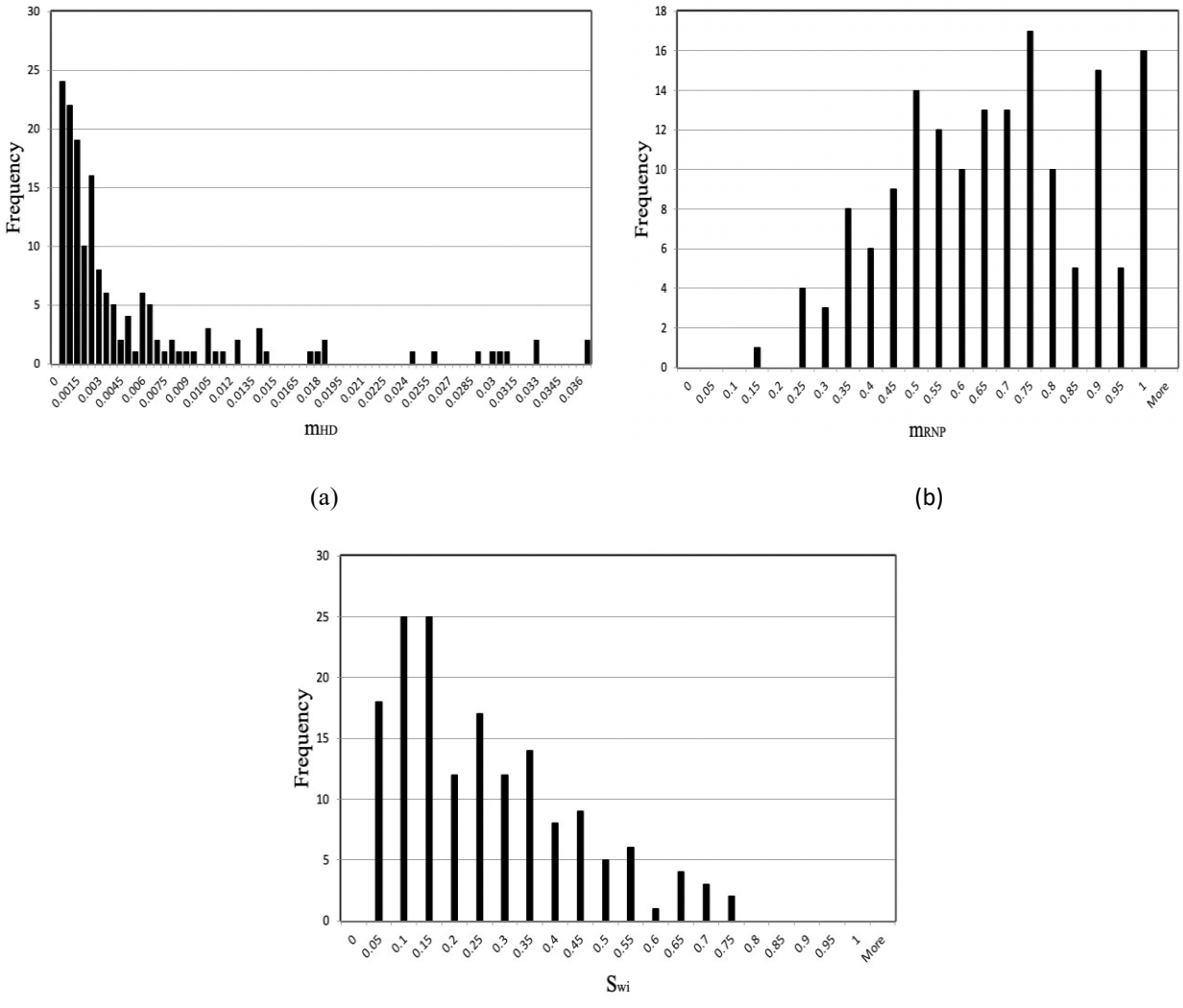

Figure 3.1: Frequency distributions of a) m_{HD}, b) m_{RNP}, and c) S_{wi} for the studied wells with both pressure and log data.

Chapter 4: Results of Case Studies 1 and 2

4.1 Introduction

The main objective of this study is to evaluate the possibility of quantifying matrix and fracturing water contributions to the total produced water based on the water flowback response. This chapter presents the results of studied wells from the Montney, Horn River, and Duvernay Formations to test the proposed hypothesises.

4.2 Results of case study 1: Oil wells completed in the Montney Formation

In this section, we test our proposed hypothesises by conducting quantitative analysis of flowback and log data for oil wells completed in the Montney Formation. The quantitative analysis involves 1) classify the studied wells based on observed m_{HD}, 2) construct RNP diagnostic plots of the studied wells, 3) investigate the relationship between m_{HD} and m_{RNP}, 4) analyze log data and estimate average initial water saturation (S_{wi}) for the studied wells, and 5) investigate the relationship between m_{HD} and S_{wi}.

4.2.1 Overview of water-flowback HD profile

The HD model can be used to describe the relationship between Q_w and water rate q_w by using the following equation (Lee and Wattenbarger 1996):

$$\ln(q_w) = \ln(q_i) - \left(\frac{D_i}{q_i}\right) Q_w \tag{4.1}$$

Therefore, the slope on the semi-log plot of q_w versus Q_w gives

$$m_{HD} = \frac{D_i}{q_i} = \frac{\ln(q_i) - \ln(q_w)}{Q_w} \tag{4.2}$$

D_i and q_i are effective water decline rate and initial water rate, respectively. Increasing the amount of matrix water influx increases q_w and Q_w, and thus, both D_i and m_{HD} decrease. Here, we

construct the semi-log plots of q_w versus Q_w and analyze the water-flowback rate-decline trends of 379 oil wells completed in the Montney Formation. All the studied wells show the HD trend during their water-flowback process. As shown in **Figure 4.1**, Well A represents the wells with higher m_{HD}, indicating less matrix water contributions. In contrast, Well B shows very low m_{HD} through the entire flowback process, indicating higher amount of water influx from the matrix into fractures. However, Well C shows an initial increasing trend for q_w until Q_w reaches to 900 m^3 then declines. We observe frequent choke-size variations from the production reports of these wells, explaining the early increasing trend of q_w. **Figure 4.1c** also shows that q_w follows the HD trend when the choke size remains constant at $50/64''$. Here, we ignore the early data, and construct RNP diagnostic plots in the next section for the Montney wells that follow HD trend.

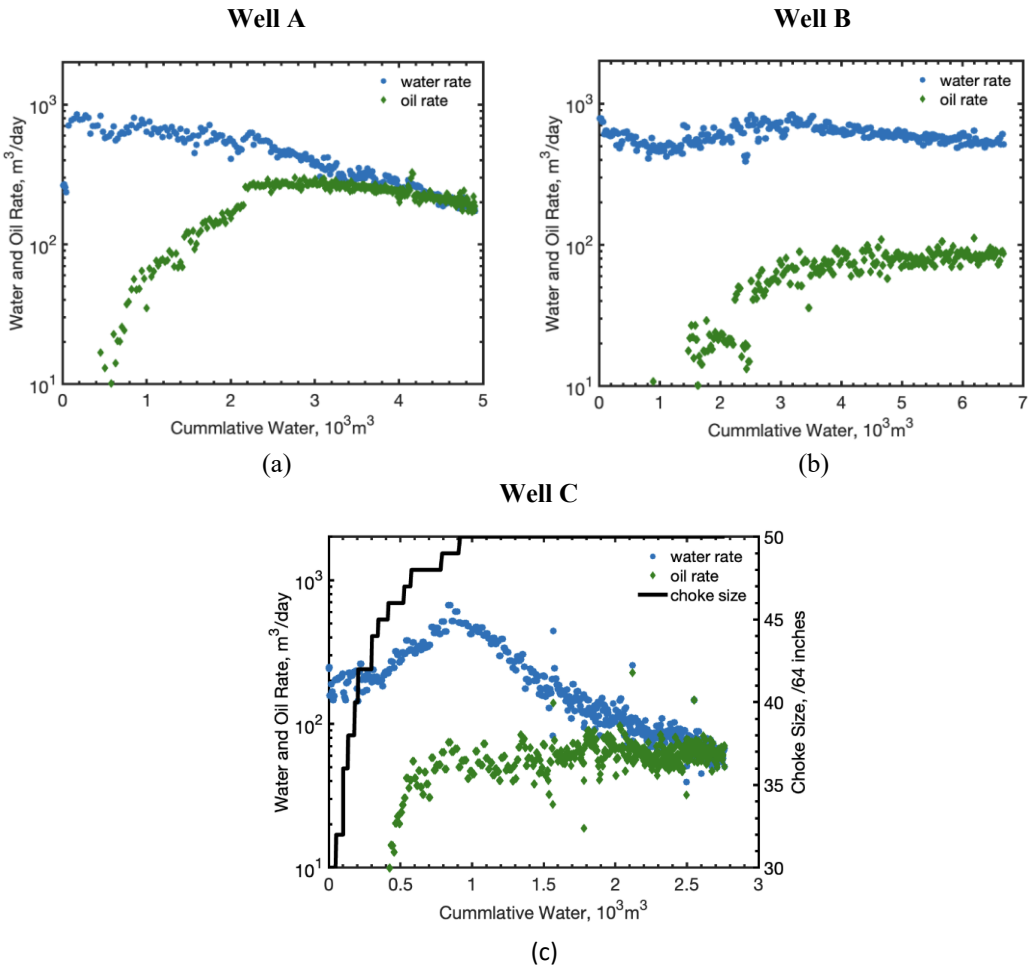

Figure 4.1: Semi-log plots of q_w and q_o versus Q_w for three sample oil wells with: a) high m_{HD}, b) low m_{HD}, and c) early increasing trend of q_w due to frequent choke size variations

4.2.2 Comparing RNP plots of the wells with high and low m_{HD}

Here, we use the available data to construct the plots of RNP versus MBT on a log-log scale (Abbasi et al. 2012). **Figure 4.2** shows RNP plots for 6 sample wells with low m_{HD} ($10^{-5}\ to\ 10^{-4}\ 1/m^3$) and the observed m_{RNP} are relatively low (0.2 to 0.6). **Figure 4.3** shows that the m_{RNP} values for another 6 wells with very high m_{HD} ($3 \cdot 10^{-3}\ to\ 10^{-2}\ 1/m^3$) are relatively higher (0.64 to 1). This observation suggests that there may exist a positive correlation between m_{HD} and m_{RNP}. Therefore, we construct a cross plot of m_{HD} versus m_{RNP} in the next section to investigate the existence of any correlations.

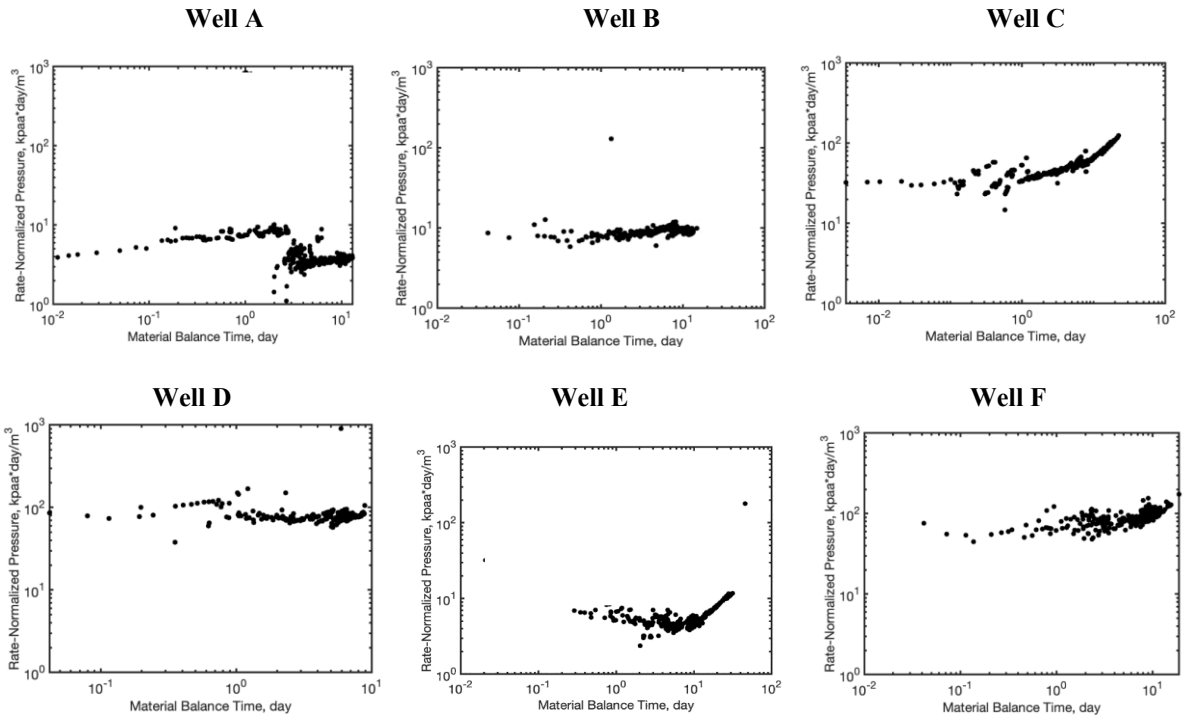

Figure 4.2:Log-log plots of RNP versus MBT for sample oil wells with lower m_{HD}.

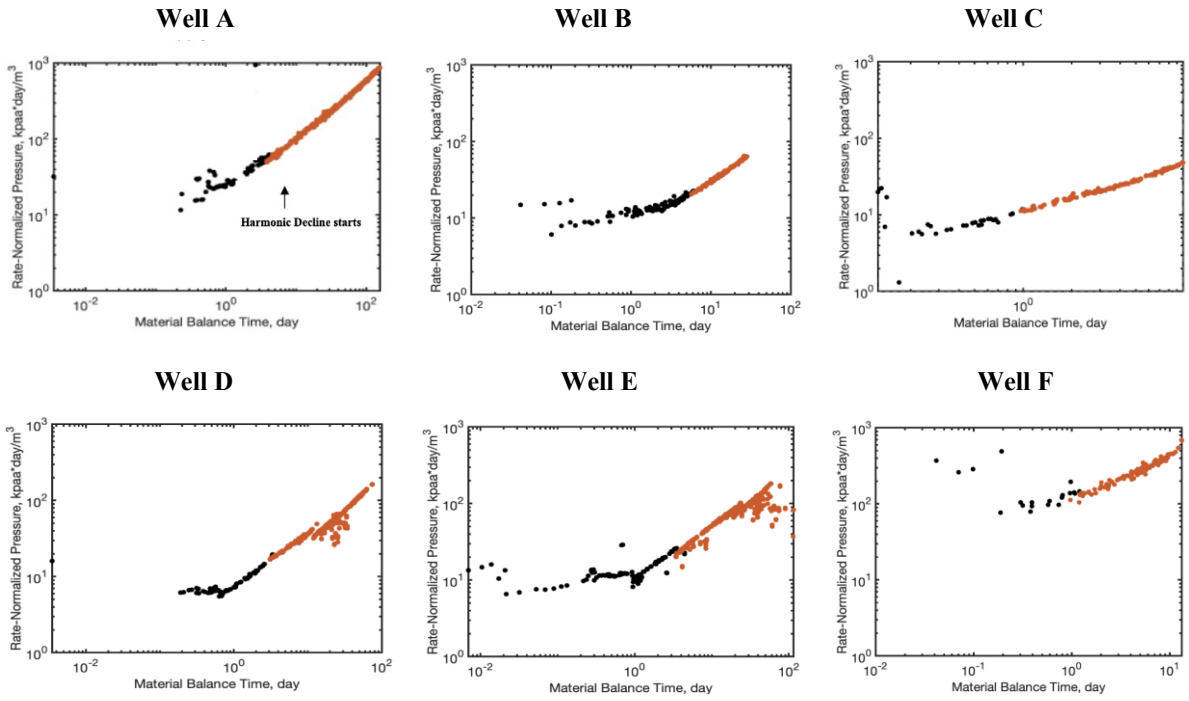

Figure 4.3: Log-log plots of RNP versus MBT for sample oil wells with higher m_{HD}
The starting points of red curves indicate the starting points of consistent linear trends on the RNP plots.

4.2.3 Correlation between m_{HD} and m_{RNP}

In this section, we test the correlation between m_{HD} and m_{RNP} for 127 of the 379 oil wells with available pressure data for the entire flowback period. **Figure 4.4** shows that m_{HD} is positively correlated with m_{RNP}. The exponential model gives the lowest root mean square error (RMSE) of 0.0022 1/day and absolute average percentage error (AAPE) of 23%, respectively, compared with the linear and power models. The exponential correlation is more obvious in the semi-log plot, as shown in **Figure 4.4b**. However, the AAPE value is still high and it will be discussed at the end of Case Study 2.

In this figure, the well with a nearly unit slope can be considered as the base case, suggesting a closed system in which the produced water mainly comes from fractures with negligible water influx from the matrix.

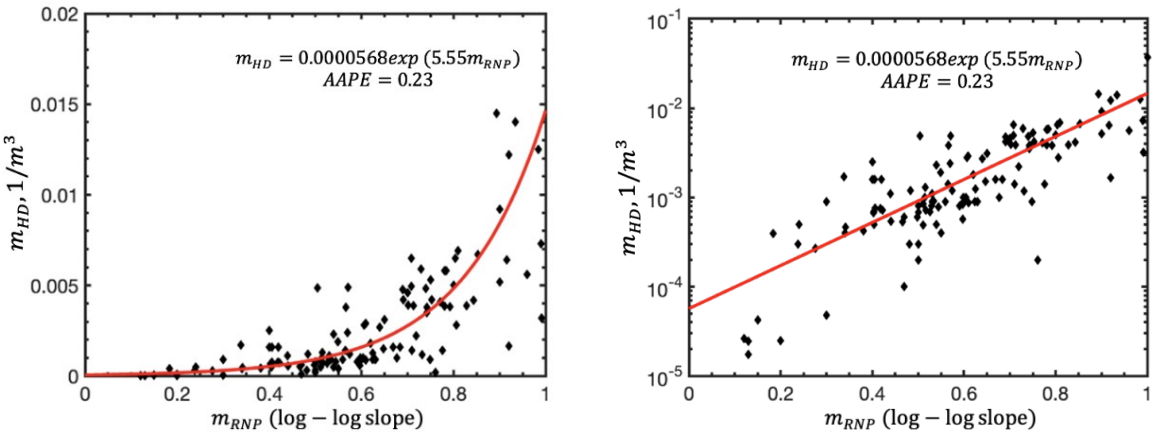

Figure 4.4: m_{HD} versus m_{RNP} for 127 Montney wells on a) cartesian plot and b) semi-log plot

For the next step, we investigate the existence of a possible correlation between m_{HD} and S_{wi}, assuming S_{wi} is proportional to the formation water influx. The water influx from the matrix into fracture is controlled by water mobility defined by

$$\lambda_w = \frac{k_{rw}}{\mu_w} \tag{4.3}$$

Here, k_{rw} is water relative permeability. Based on the relative permeability curve, formation water is mobile if the initial water saturation (S_{wi}) is higher than connate water saturation (S_{wc}). μ_w is water viscosity and its value mainly depends on the reservoir temperature and pressure (Likhachev et al. 2003). In this study, water mobility is hard to estimate due to the unavailability of core analysis data of the studied wells, and we cannot obtain the water relative permeability curves. In the modified Brooks-Corey model (1964), water relative permeability is defined by

$$k_{rw} = k_{rw,max} \cdot \left(\frac{S_w - S_{wc}}{1 - S_{or} - S_{wc} - S_{gc}}\right)^{n_w} \tag{4.4}$$

Here, $k_{rw,max}$ is the maximum water relative permeability, S_{wc} is the connate water saturation, S_{or} is the residual oil saturation, S_{gc} is the critical gas saturation, and n_w is water exponent. In this model, these parameters only depend on the fluid and rock properties. Therefore, we assume

that the initial formation water mobility is proportional to S_{wi}. The methodology for estimating S_{wi} and its correlation with m_{HD} will be presented in the next section.

4.2.4 S_{wi} estimation by using well-log data

We estimate the average S_{wi} of each well by using the available log data. The Simandoux model (1963) is used to account for the clay effect on calculated S_{wi}:

$$S_{wi} = \left(\frac{R_w}{\emptyset^m \cdot 2}\right) \cdot \left[\sqrt{\left(\frac{V_{sh}}{R_{sh}}\right)^2 + \frac{4\emptyset^m}{R_w \cdot R_t}} - \frac{V_{sh}}{R_{sh}}\right] \quad (4.5)$$

Here, m is the cementation component with a typical value of 1.7 for sand with clay minerals. R_w is water resistivity, which is obtained from the available fluid analysis reports. R_t is true resistivity and it is obtained from the corresponding deep resistivity log. $\emptyset$ is the porosity of the rock matrix. We use density porosity in the sandstone unit as approximate true matrix density to calculate the porosity of the rock matrix at the average measured depth of fracture stages. However, the formations may be very heterogeneous and the rock types may not be the same for all the studied wells. The calculated density porosity is very sensitive to the assumed matrix density, and this leads to errors in S_{wi} estimation. V_{sh} and R_{sh} are shale volume fraction and shale resistivity respectively. V_{sh} is obtained from the gamma ray log data. Total gamma ray may overestimate V_{sh} since organic materials may lead to high values of Uranium content (Erickson et al.1954). In this case, overestimating V_{sh} leads to underestimation of S_{wi}. R_{sh} is obtained from the deep resistivity log of the section which has very high gamma-ray value. Thus, this approach requires us to assume that 1) the section which shows the highest gamma-ray value is a shale layer and 2) the section which shows the lowest gamma-ray value represents a relatively clean zone with negligible shale content, as shown in **Figure A-1** in Appendix A as an example.

The objective of this analysis is just to approximately estimate and compare S_{wi} of different wells, and to investigate its relationship to m_{HD}. Therefore, we used approximate average values for the parameters in the Simandoux model. The errors and uncertainties will be discussed in the "**Uncertainties and limitations**" section.

4.2.5 Correlation between m_{HD} and S_{wi}

Among the 379 oil wells, only 100 wells have the log data to estimate S_{wi} and to find its correlation with m_{HD}. **Figure 4.5** shows that m_{HD} inversely correlates with S_{wi}. The exponential model shows the lowest RMSE of 0.0027 $1/m^3$ compared with linear and power models. m_{HD} decreases by increasing S_{wi}, suggesting lower m_{HD} for wells with higher formation water mobility. The observed correlation shows that the formation water mobility is proportional to the estimated S_{wi} assuming that the studied wells are completed in the same formation and have similar rock properties. The exponential model still gives us a high RMSE value due to the high variations of well-completion data and uncertainties involved in S_{wi} estimation.

Next, we construct the same cross plot for 25 sample oil wells. **Table 4.1** lists the key completion parameters for these wells: 1) number of fracture stages ranging from 21 to 32, 2) well choke size ranging from 45 to 50 *in*, 3) well true vertical depth (TVD) ranging from 1961 to 2454 *m*, 4) flowback duration ranging from 9 to 15 days, and 5) total water injection volume (TIV) ranging from 8706 to 28092 m^3. We observed that only TIV has a significantly high variation while the other parameters are similar for these studied wells. **Figure 4.6a** still shows that m_{HD} is inversely correlated with S_{wi}. As we expected, the fitted linear model gives a low AAPE value and significantly lower RMSE of 0.00011 $1/m^3$ compared with RMSE of 0.0027 $1/m^3$ in the previous model.

Since higher S_{wi} indicates lower m_{HD} during water flowback, Q_w at the end of flowback is expected to be higher for wells with higher S_{wi} assuming that the wells have similar completion parameters. Since TIV has high variations, Q_w is normalized by TIV, which is defined as water load recovery (LR). As shown in **Figure 4.6b**, LR is positively correlated with S_{wi}. Here, the values of LR are estimated and compared after the same flowback duration (9 days).

In this case study, we analyzed 379 oil wells from the Montney Formation. However, only 100 wells had both pressure and log data. In the next case study, we conduct the same methodology to analyze more oil wells from the Horn River and Duvernay formations. Then, we propose a method to determine separately the volume of produced fracturing and matrix water during flowback.

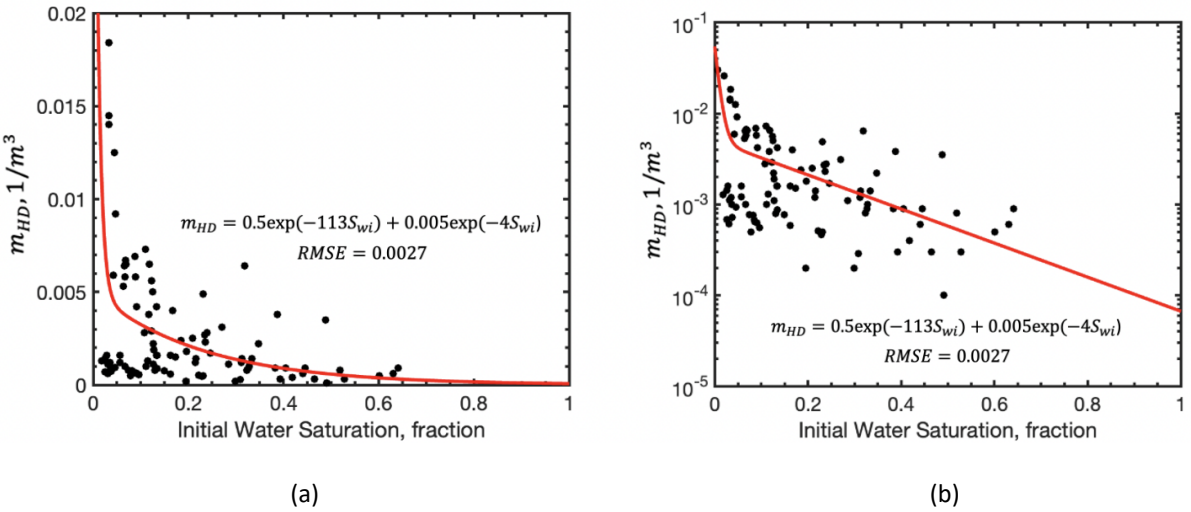

Figure 4.5: m_{HD} versus S_{wi} for 100 Montney wells on a)cartesian plot and b) semi-log plot

Table 4.1: Key completion parameters for 25 oil wells from the Montney Formation

Well Completion	
Formation name	Montney Formation
Number of wells	25
Choke size, in	45-50
Number of fracture stages	21-32
TVD, m	1961-2454
TIV, m^3	8706-28092
Flowback duration, day	9-15

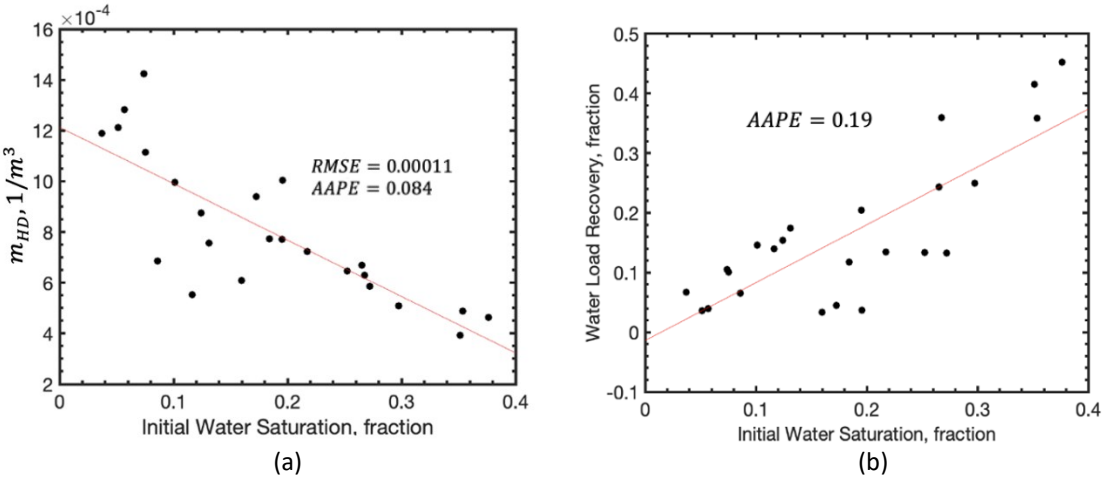

Figure 4.6: a) m_{HD} and b) water load recovery versus S_{wi} for 25 Montney wells with similar completion parameters

4.3 Results of case study 2: Oil and gas wells from Horn River and Duvernay Formations

In pervious case study, we analyzed 379 oil wells from the Montney Formation. However, only 100 wells had both pressure and log data. In this case study, we conduct the same methodology to analyze more wells from the Horn River and Duvernay formations. Then, we proposed a method to determine the volume of produced fracturing water and matrix water during flowback.

4.3.1 Correlation between m_{HD} and m_{RNP}

In this case study, we conduct the same quantitative analysis for additional 89 wells from the Duvernay and Hover River formations to investigate the general relationship between m_{HD} and m_{RNP}. Therefore, the studied sample includes 1) 40 oil and gas wells from the Horn River Formation, 2) 49 oil wells from the Duvernay Formation, and 3) the previous 127 oil wells from the Montney Formation. **Figure 4.7** shows plots of m_{RNP} versus m_{HD} for these studied wells on cartesian and semi-log coordinates. The exponential model gives the lowest RMSE of 0.0031 $1/m^3$ and AAPE of 37% compared with linear and power models. In general, there is a positive correlation between m_{HD} and m_{RNP}. The observed general positive correlation suggests that the wells with higher m_{RNP} have lower water influx from their matrix system into fractures. Furthermore, wells with lower m_{RNP} are expected to have higher water influx, and thus, their m_{HD} is lower.

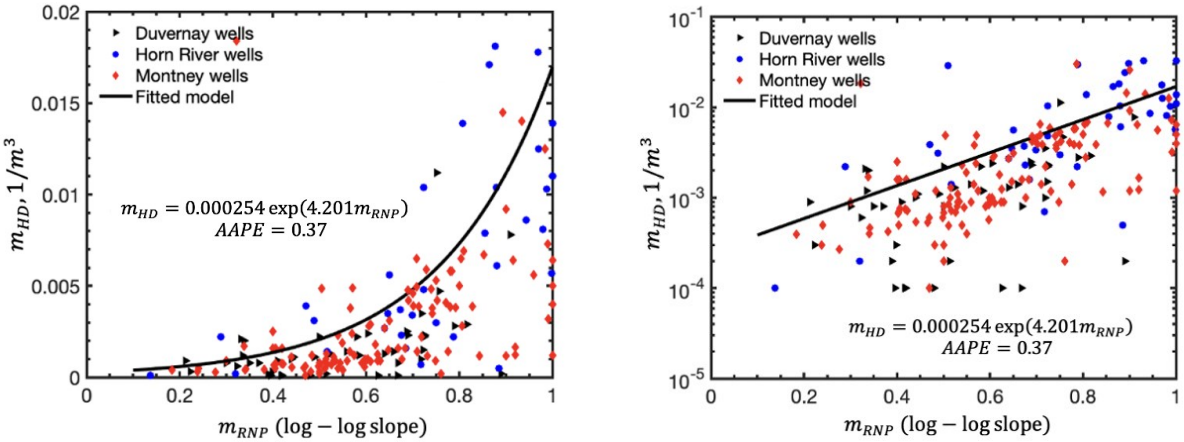

Figure 4.7: m_{HD} versus m_{RNP} on a) cartesian plot and b) semi-log plot for the 216 studied wells

4.3.2 Correlation between m_{HD} and S_{wi}

The amount of formation water influx is proportional to S_{wi} assuming that the studied wells have similar rock properties. Here, we analyzed the log data to test the correlation between m_{HD} and S_{wi} of the studied wells, including 1) 40 wells from the Horn River Formation, 2) 49 wells from the Duvernay Formation, and 3) 100 wells from the Montney Formation with available log data from the previous case study. **Figure 4.8** shows m_{HD} versus S_{wi} for the total of 189 oil and gas wells from 3 different formations with HD trend of water-flowback. The exponential model still gives the lowest RMSE of 0.0029 $1/m^3$ and AAPE of 33.4% compared with linear and power models. Although the data are scattered, in general, there is a negative correlation between m_{HD} and S_{wi}.

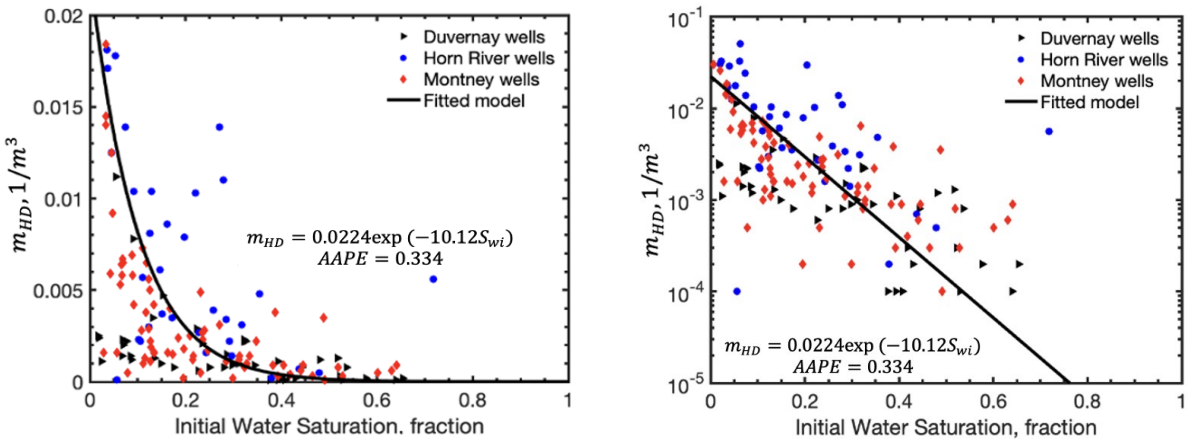

Figure 4.8: m_{HD} versus S_{wi} on a) cartesian plot and b) semi-log plot for the 189 studied wells

From both case studies, we observe the approximate exponential trends on both cartesian plots of m_{HD} versus m_{RNP} and m_{HD} versus S_{wi}. For wells with high m_{RNP} and low S_{wi}, water is mainly produced from fractures. In such case, the completion parameters significantly affect m_{HD}. Therefore, wells with different completion parameters show high variations in m_{HD}. The values of

AAPE for the exponential models are high, ranging from 23% to 37% due to variations in well completion parameters, well geometries, and uncertainties involved in S_{wi} estimation.

4.4 Estimating fracturing and formation water production during water-flowback process

For the studied wells, both core analysis and water chemical data are unavailable. Therefore, it is hard to estimate the actual produced volumes of fracturing and matrix water. However, the results from the two case studies suggest that both m_{RNP} and m_{HD} can be interpreted as a signature of formation water mobility and water breakthrough, especially for the wells completed in the same formation with similar rock properties. In this section, we propose a new heuristic model and an analysis procedure to approximately estimate 1) instantaneous fracturing water (q_w^f) and matrix water rate (q_w^{ma}), 2) cumulative fracturing water (Q_w^f) and matrix water production (Q_w^{ma}) during water-flowback process.

4.4.1 Analysis procedure of the heuristic model

Here, we use RNP diagnostic plots because 1) m_{HD} shows high variations for wells with different completion parameters and well geometries, and 2) m_{RNP} has a threshold value of 1 at very early time indicating negligible water influx from matrix.

This proposed model is based on the following assumptions:

1) Wells with negligible water influx from the matrix start to show a unit slope at very early time of flowback processes (MBT=1 day) on log-log RNP plot.
2) There is no leak-off of fracturing water from fractures into matrix.
3) There is no well interference during the entire flowback process.

4) There is no change in m_{RNP} during the flowback process.

In this study, water RNP is given by

$$RNP = \frac{P_i - P_{wf}}{q_w^s} \tag{4.4}$$

Next, we define RNP_{wf} as

$$RNP_{wf} = \frac{P_i - P_{wf}}{q_w^f} \tag{4.5}$$

Here, P_i and P_{wf} are initial fracture pressure and well bottomhole pressure. q_w^f is the surface flowrate (q_w^s) in the absence q_w^{ma}. Therefore, q_w^f and q_w^{ma} are given by

$$q_w^f = \left(\frac{RNP}{RNP_{wf}}\right) \cdot q_w^s \text{ and, } q_w^{ma} = q_w^s - q_w^f \tag{4.6}$$

Q_w^f and Q_w^{ma} are given by

$$Q_w^f = q_w^f \cdot MBT \text{ and, } Q_w^{ma} = Q_w - Q_w^f \tag{4.7}$$

Next, we propose the following analysis procedure to approximately differentiate between fracturing and matrix water recovery without the analysis of water chemical data:

1) Obtain flowback pressure and rate data.

2) Construct water RNP versus MBT on cartesian plot.

3) Ignore the early noisy data, and determine m_{RNP} using the best linear match.

4) Determine the intercept C on the cartesian plot.

5) Construct water RNP versus MBT on log-log plot.

6) Draw a linear line from the intercept C on cartesian plot until the line start to show a unit slope at early time of flowback processes (MBT=1 day) on corresponding log-log RNP plot. This line approximately represents RNP_{wf} versus MBT for the studied wells.

7) Calculate the ratio between RNP and RNP_{wf}.

8) Estimate q_w^f, q_w^{ma}, Q_w^f, Q_w^{ma} during water-flowback processes.

4.4.2 Example applications

Figure 4.9 shows RNP versus MBT for a sample oil well on log-log and cartesian plots. The best linear match shows an m_{RNP} value of 6.2 $kpa \cdot day/m^3$ (log-log slope of 0.7) and a C value of 20.06 $kpa \cdot day/m^3$, indicating matrix water influx during the flowback process. Then, we draw a linear line from the intercept until the line start to show a unit slope at early time of flowback processes on corresponding log-log RNP plot. This line represents RNP_{wf} versus MBT under 1) the same bottomhole pressure, 2) the same fracture and matrix properties, and 3) the same well geometry for this sample well. Therefore, the fracturing and matrix water contributions during water-flowback processes can be approximately estimated using Eq. 4.4 to Eq. 4.7.

Figure 4.10 shows the semi-log plot of estimated water flowrates (q_w, q_w^f, q_w^{ma}) versus Q_w for this sample well. The matrix contribution to the total produced water increases with time. At very early time, q_w^f dominates water production. During the late water-flowback period, q_w^{ma} dominates water production. In this case, the total produced volume of flowback-water is recorded as 1400 m^3. The estimated total produced volumes of fracturing water and formation water are 600m^3 and 800m^3, respectively. Other 3 example applications are presented in Appendix B.

Overall, the applications of our model on field data shows 1) Q_w^f dominates the total water recovery for wells with higher m_{RNP}, and 2) Q_w^{ma} dominates the total water recovery for wells with lower m_{RNP}.

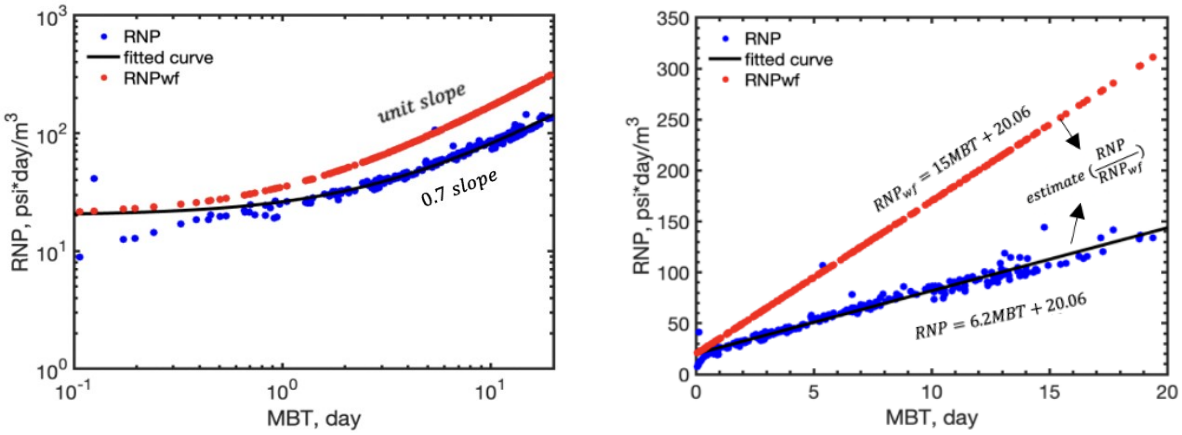

(a) (b)

Figure 4.9: RNP versus MBT for a sample oil well on a) log-log plot and b) cartesian plot

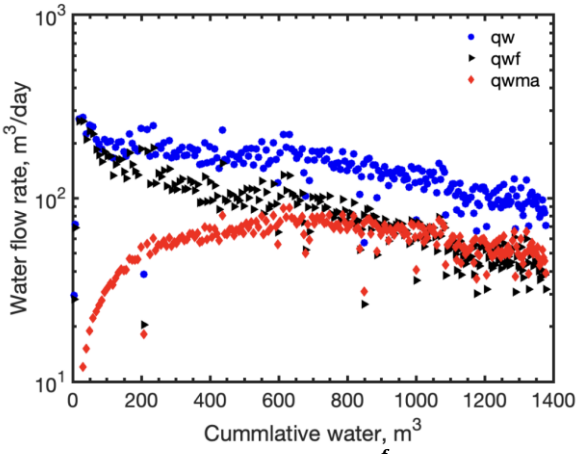

Figure 4.10: Semi-log plots of calculated q_w, q_w^f, and q_w^{ma} versus Q_w for a sample oil well

Table 4.2: Calculated values for Q_w^{ma} and Q_w^f at the end of the flowback process for the sample oil well

Q_w m^3	AAPE, fraction	Q_w^f m^3	Q_w^{ma} m^3	TIV m^3	Q_w/TIV fraction	Q_w^f/TIV fraction	Q_w^{ma}/TIV fraction
1400	0.084	600 ± 50.4	800 ± 67.2	8200	0.171	0.073 ± 0.006	0.098 ± 0.008

Chapter 5: Theoretical analysis and Heuristic Model for Estimating Formation and Fracturing Water Contributions during Water-flowback Processes

5.1 Introduction

In this section, we present theoretical analyses to further test the proposed hypotheses. The uncertainties and limitations in this study are also summarized.

5.2 Pseudo steady-state (PSS) solution of water RNP diagnostic plot

Abbasi et al (2014) proposed two models for estimating fracture properties by analyzing single-phase water flowback assuming radial and linear flow through hydraulic fractures. Here, we extend their radial flow model by considering the water influx from the stimulated matrix into fractures.

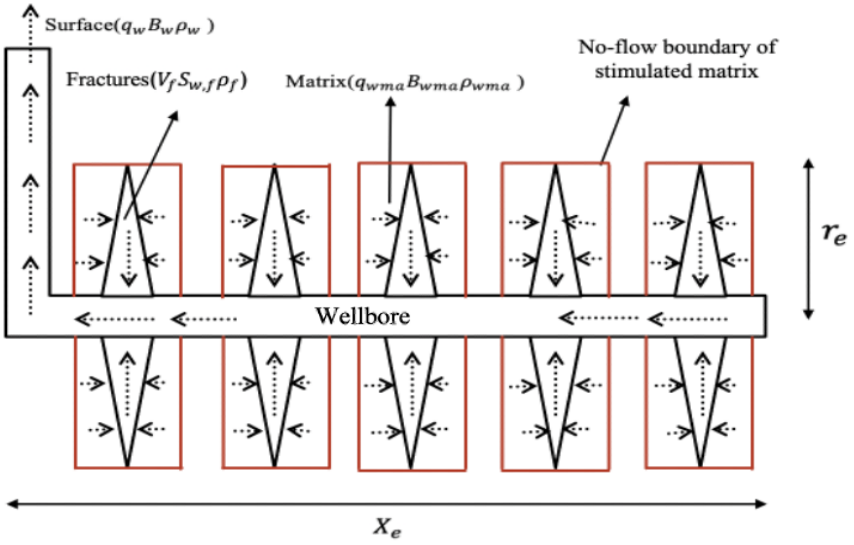

Figure 5.1: 2-D view of a fractured horizontal well. The black arrows show the flow direction of water in fractures and in stimulated matrix. The red lines represent no-flow boundaries of stimulated matrix.

Firstly, we treat hydraulic fractures and wellbore including horizontal and vertical sections as the "**control volume**". The material balance equation is given by

Mass in – Mass out = Acclamation (5.1)

$$q_w^{ma} B_w^{ma} \rho_w^{ma} - q_w^s B_w^s \rho_w^s = \frac{d}{dt}(\rho_w^f V_f \emptyset_f \bar{S}_w^f + \rho_w^{wb} V_{wb}) \quad (5.2)$$

Here, q represents flowrate, B represents the formation volume factor, ρ is density, V is volume, and $\emptyset$ is porosity. Scripts *w, s, ma, f* and *wb* denote water, surface, stimulated matrix, fractures and wellbore, respectively. In this study, the produced flowback-water includes fracture water and matrix water. Note that $\bar{S}_w^f$ is average water saturation in fractures over flowback period. We make the following assumptions:

- We assume the permeability of formation (unstimulated matrix) is much lower than that of the stimulated matrix, and thus, this is no flow and pressure communication between formation and the stimulated matrix (no flow conditions at the borders of the red boxes).
- There is no interference between the fracture stages. This assumption also means the width of the red boxes cannot be very large.
- q_w^{ma} represents water influx from the stimulated matrix into the fractures.
- The effective radius of the stimulated matrix is almost equal to the equivalent fracture radius (r_e), as shown in **Figure 5.1**.
- $B_w^s = B_w^{ma} = B$, meaning that the thermodynamic conditions at the surface is the same as that in the stimulated matrix.
- $\rho_w^s = \rho_w^{ma} = \rho_w^f = \rho_w^{wb}$. This assumption means that the average density of total produced flowback water on the surface, that of water recovered from the matrix, the fractures, and the wellbore are almost equal.
- $\frac{dP_{wb}}{dt} = \frac{dP_f}{dt} = \frac{\partial P_{ma}}{\partial t} = \frac{\partial \bar{P}}{\partial t}$. Here, P_{wb}, P_f, and P_{ma} are average pressure in the wellbore, fractures, and matrix, respectively. This assumption means that the rate of change of average

pressure with respect to time in the wellbore is almost the same as that in the fractures, the stimulated matrix, and is given by average pressure drop. This assumption also means the whole system is under pseudo steady-state conditions.

Following the derivation procedure of Abbasi et al (2014), the material balance equation gives

$$\frac{d\bar{P}}{dt} = \frac{(q_w^{ma} - q_w^s)\cdot B}{C_{st}} \tag{5.3}$$

Then, we define $q_w^f = q_w^s - q_w^{ma}$ (5.4)

Here, q_w^f is the surface flowrate in the absence of water influx from the matrix. Substituting Eq. 5.4 into Eq. 5.3 gives

$$\frac{d\bar{P}}{dt} = \frac{-q_w^f \cdot B}{C_{st}} \tag{5.5}$$

where, $C_{st} = \frac{dV_f}{dP}\bar{S}_w^f\bar{\emptyset}_f + \bar{V}_f\bar{\emptyset}_f\bar{C}_t^f\bar{S}_w^f + V_{wb}C_w^{wb}$. (5.6)

Here, C is compressibility and C_{st} is total water storage coefficient of the wellbore and fractures. $\frac{dV_f}{dP}$ accounts for fracture closure as pressure drops during water-flowback. The second and third term on the right hand side represent water storage in fracture and wellbore, respectively.

Integrating Eq. 5.5 and rearranging, gives

$$\bar{P}(t) = P_i - \frac{Q_w^f B}{C_{st}} \tag{5.7}$$

where, P_i and Q_w^f represent initial fracture pressure and the cumulative fracture water production, respectively.

Next, we consider the radial flow of fracture water and matrix water through hydraulic fractures towards the wellbore. The previously proposed model (Abbasi et al. 2014) assumes negligible water influx from matrix into fractures, and is given by

$$\frac{\bar{K}_w^f}{\mu}\frac{1}{r}\left(\frac{\partial}{\partial r}\right)\left(r\frac{\partial P_f}{\partial r}\right) = \bar{\emptyset}_f \bar{C}_t^f \bar{S}_w^f \frac{\partial P_f}{\partial t} \tag{5.8}$$

Here, we use $\bar{K}_w^f$ instead of K_f in previous model, and it represents the average effective permeability of water in fractures over flowback period. Water material balance equation in the stimulated matrix is given by

$$0 - q_w^{ma}\rho_w^{ma} = \bar{S}_w^{ma}\frac{\partial(\emptyset_{ma}V_{ma}\rho_w^{ma})}{\partial t} \tag{5.9}$$

Here, $\bar{S}_w^{ma}$ is average water saturation in the stimulated matrix over flowback period. We assume constant volume of the stimulated matrix with respect to time. Rearranging Eq. 5.9 gives

$$-q_w^{ma}\rho_w^{ma} = V_{ma}\bar{S}_w^{ma}\frac{\partial(\emptyset_{ma}\rho_w^{ma})}{\partial t} \tag{5.10}$$

Eq. 5.10 can be simplified by using the chain rule

$$-q_w^{ma}\rho_w^{ma} = \emptyset_{ma}V_{ma}\bar{S}_w^{ma}\rho_w^{ma}\frac{1}{\rho_w^{ma}}\frac{\partial(\rho_w^{ma})}{\partial Pma}\frac{\partial Pma}{\partial t} + \emptyset_{ma}V_{ma}\bar{S}_w^{ma}\rho_w^{ma}\frac{1}{\emptyset_{ma}}\frac{\partial(\emptyset_{ma})}{\partial Pma}\frac{\partial Pma}{\partial t} \tag{5.11}$$

By considering the definition of isothermal compressibility for pores (C_p^{ma}) and water (C_w^{ma}) in the matrix, Eq. 5.11 can be rewritten as

$$-q_w^{ma}\rho_w^{ma} = \emptyset_{ma}V_{ma}\bar{S}_w^{ma}\rho_w^{ma}C_w^{ma}\frac{\partial Pma}{\partial t} + \emptyset_{ma}V_{ma}\bar{S}_w^{ma}\rho_w^{ma}C_p^{ma}\frac{\partial Pma}{\partial t} \tag{5.12}$$

Dividing both sides by $\rho_w^{ma}V_f$, gives

$$-\frac{q_w^{ma}}{V_f} = \frac{V_{ma}}{V_f}\emptyset_{ma}C_t^{ma}\bar{S}_w^{ma}\frac{\partial Pma}{\partial t} \tag{5.13}$$

where, $C_t^{ma} = C_w^{ma} + C_p^{ma}$

The term q_w^{ma}/V_f represents the normalized water influx from matrix into fractures. C_t^{ma} is the total compressibility in the stimulated matrix. Next, we consider q_w^{ma}/V_f as a source term and combine Eq. 5.13 and Eq. 5.8 to arrive at

$$\frac{\bar{K}_w^f}{\mu}\frac{1}{r}\left(\frac{\partial}{\partial r}\right)\left(r\frac{\partial P_f}{\partial r}\right) = \bar{\emptyset}_f \bar{C}_t^f \bar{S}_w^f \frac{\partial P_f}{\partial t} + \frac{V_{ma}}{V_f}\emptyset_{ma}C_t^{ma}\bar{S}_w^{ma}\frac{\partial Pma}{\partial t} \tag{5.14}$$

The proposed dual-porosity involves the following assumptions:

- Constant porosity ($\emptyset$) and total compressibility (C_t) with respect to time in the stimulated matrix.
- Constant temperature and viscosity (μ) of water in fractures and matrix.
- $\frac{dP_{wb}}{dt} = \frac{dP_f}{dt} = \frac{\partial P_{ma}}{\partial t} = \frac{\partial \bar{P}}{\partial t}$.

Rearranging Eq. 5.14 gives

$$\frac{1}{r}\left(\frac{\partial}{\partial r}\right)\left(r\frac{\partial P_f}{\partial r}\right) = \frac{(\bar{\emptyset}_f \bar{C}_t^f \bar{S}_w^f + VR \cdot \emptyset_{ma} C_t^{ma} \bar{S}_w^{ma})\mu}{\bar{K}_w^f}\frac{\partial P_f}{\partial t} \tag{5.15}$$

$$\text{where, } VR = \frac{V_{ma}}{V_f} \tag{5.16}$$

Here, VR is the bulk volume ratio between fractures and stimulated matrix. Eq. 5.15 can be solved under the same boundary conditions and following the radial flow procedure proposed by Abbasi et al (2014). The final generalized solution for average fracture pressure as a function of time is given by

$$P(t) = P_{wf} + \frac{(\bar{\emptyset}_f \bar{C}_t^f \bar{S}_w^f + VR \cdot \emptyset_{ma} C_t^{ma} \bar{S}_w^{ma})\mu}{\bar{K}_w^f}\frac{q_w^f B}{2C_{st}} r_e^2 \left[\frac{1}{2}\ln\left(\frac{4A}{C_A \gamma r_w^2}\right)\right] \tag{5.17}$$

Here, P_{wf} is well bottomhole pressure, A represents the area of the vertical section of the fractures, r_e represents equivalent fracture radius, and C_A is the fracture shape factor. Substituting Eq. 5.7 into Eq. 5.17, and dividing both sides by $q_w^f B$, gives:

$$\frac{P_i - P_{wf}}{q_w^f} = \frac{Q_w^f B}{q_w^f C_{st}} + \frac{(\bar{\emptyset}_f \bar{C}_t^f \bar{S}_w^f + VR \cdot \emptyset_{ma} C_t^{ma} \bar{S}_w^{ma})B\mu}{2C_{st}\bar{K}_w^f} r_e^2 \left[\frac{1}{2}\ln\left(\frac{4A}{C_A \gamma r_w^2}\right)\right] \tag{5.18}$$

Here, $(P_i - P_{wf})/\, q_w^f$ is referred to as fracturing water rate-normalized pressure (RNP_{wf}) and Q_w^f/q_w^f is referred to as MBT:

$$RNP_{wf} = \frac{P_i - P_{wf}}{q_w^f} = \frac{B}{C_{st}} MBT + C \tag{5.19}$$

where, C = $\frac{(\bar{\emptyset}_f \bar{C}_t^f \bar{S}_w^f + VR \cdot \emptyset_{ma} C_t^{ma} \bar{S}_w^{ma}) B\mu}{2 C_{st} \bar{K}_w^f} r_e^2 \left[\frac{1}{2} \ln\left(\frac{4A}{C_A \gamma r_w^2}\right)\right]$

The slope is given by

$$m_{RNP_{wf}} = \frac{B}{C_{st}} = \frac{B}{\frac{dV_f}{dP} \bar{S}_w^f \bar{\emptyset}_f + \bar{V}_f \bar{\emptyset}_f \bar{C}_t^f \bar{S}_w^f + V_{wb} C_w^{wb}} \tag{5.20}$$

Figure 5.2 shows the sensitivity test of m_{RNPfw} by changing VR. The matrix properties have no effects on m_{RNPfw}. However, they affect C, and affect the time to observe a unit slope on the log-log plot of RNP_{wf} versus MBT.

Table 5.1: Assumed values of each parameter in m_{RNPwf} model

System parameters	Assumed values
$B, m^3/m^3$	1.02
$\bar{C}_t^f, 1/kpa$	$3 \cdot 10^{-4}$
$\bar{\emptyset}_f, fraction$	0.7
$\bar{S}_w^f, fraction$	0.5
$\bar{V}_f, m^3$	15000
$C_t^{ma}, 1/kpa$	$3 \cdot 10^{-5}$
$\emptyset_{ma}, fraction$	0.08
$\bar{S}_w^{ma}, fraction$	0.4
$VR, fraction$	0
$\mu, kpa \cdot day$	$1.7 \cdot 10^{-11}$
$\bar{K}_w^f, m^2$	$5 \cdot 10^{-13}$
r_e, m	6
$C_A (Rectangular\ shape)$	21.8369
γ	1.781
r_w, m	0.1
$C, kpa \cdot day/m^3$	0.144
$C_{st} \approx \bar{V}_f \bar{\emptyset}_f \bar{C}_t^f \bar{S}_{fw}^f, m^3/kpa$	1.58
$m_{RNP_{wf}} = \frac{B}{C_{st}}, kpa/m^3$	0.65 (base case)

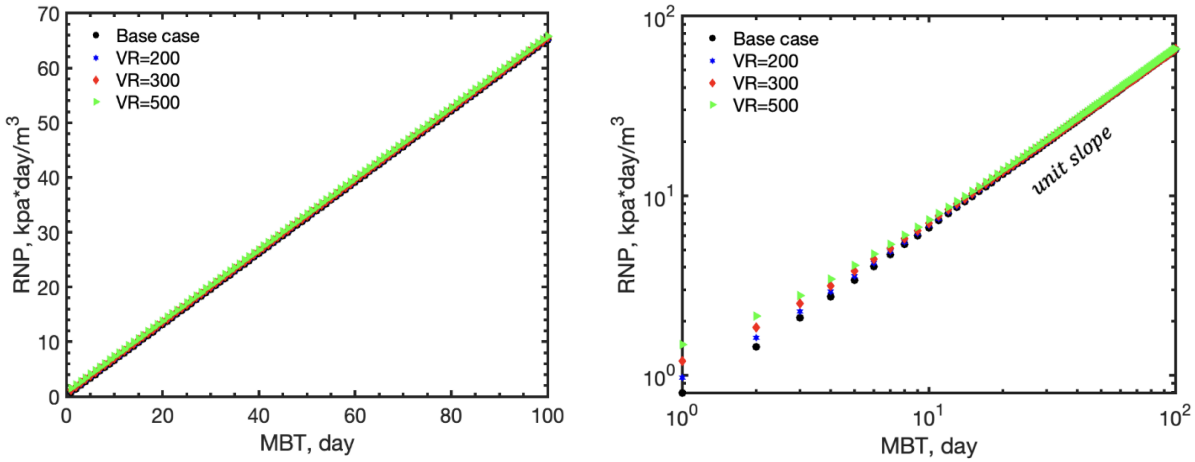

Figure 5.2: Effects of increasing VR on a) cartesian plot, and b) log-log plot of RNP_{wf} versus MBT.

In this study, $q_w^s = q_w^f + q_w^{ma}$ and RNP actually represents $(P_i - P_{wf})/\, q_w^s$. Now, we treat the whole system (wellbore, hydraulic fractures, and stimulated matrix) as the new "**control volume**". The material balance equation is given by

$$0 - q_w^s B_w^s \rho_w^s = \frac{d}{dt}(\rho_{fw}^f V_f \emptyset_f \bar{S}_w^f + \rho_w^{ma} V_{ma} \emptyset_{ma} \bar{S}_w^{ma} + \rho_w^{wb} V_{wb}) \tag{5.21}$$

Therefore, the material balance equation gives

$$\frac{d\bar{P}}{dt} = \frac{-q_w^s \cdot B}{C_{st}} \tag{5.22}$$

where, $C_{st}^{sys} = \frac{dV_f}{dP}\bar{S}_w^f \bar{\emptyset}_f + \bar{V}_f \bar{\emptyset}_f \bar{C}_t^f \bar{S}_w^f + V_{wb} C_w^{wb} + V_{ma} \emptyset_{ma} C_t^{ma} \bar{S}_w^{ma}$. (5.23)

Here, C_{st}^{sys} is total water storage coefficient of the whole system. Following the same derivation procedure (Eq. 5.7 to 5.17), the final generalized solution of average fracture pressure as a function of time is given by

$$RNP = \frac{P_i - P_{wf}}{q_w^s} = \frac{B}{C_{st}^{sys}} MBT + C \tag{5.24}$$

where, $C = \frac{(\bar{\emptyset}_f \bar{C}_t^f \bar{S}_w^f + VR \cdot \emptyset_{ma} C_t^{ma} \bar{S}_w^{ma}) B\mu}{2 C_{st}^{sys} \bar{K}_w^f} r_e^2 \left[\frac{1}{2} \ln\left(\frac{4A}{C_A \gamma r_w^2}\right)\right]$

Also, the slope on water RNP diagnostic plot in this study is given by

$$m_{RNP} = \frac{B}{C_{st}^{sys}} = \frac{B}{\frac{dV_f}{dP}\bar{S}_w^f\bar{\emptyset}_f + \bar{V}_f\bar{\emptyset}_f\bar{C}_t^f\bar{S}_w^f + V_{wb}C_w^{wb} + V_{ma}\emptyset_{ma}C_t^{ma}\bar{S}_w^{ma}} \tag{5.25}$$

Figure 5.3 shows the sensitivity test of m_{RNP} by increasing VR. The matrix properties have no effects on C in Eq. 5.24. However, they affect C_{st}^{sys}, and thus, affect m_{RNP}. We also observe that increasing VR increases the time to observe a unit slope on the corresponding log-log plot of RNP versus MBT. The flowback period usually ranges from 10 to 30 days, and thus, we can observe more derivations from a unit slope when the water influx from the matrix increases.

Negligible water influx from the matrix blocks into fractures (base case) reveals 1) $VR = 0$, 2) $q_w^f = q_w^s$, 3) $C_{st} = C_{st}^{sys}$. In this case, a unit slope will be observed at early time of flowback processes, as shown in **Figure 5.2b** and **Figure 5.3b**.

Table 5.2: Assumed values of each parameter in m_{RNP} model

System parameters	Assumed values
$B, m^3/m^3$	1.02
$\bar{C}_t^f, 1/kpa$	$3 \cdot 10^{-4}$
$\bar{\emptyset}_f, fraction$	0.7
$\bar{S}_w^f, fraction$	0.5
$\bar{V}_f, m^3$	15000
$C_t^{ma}, 1/kpa$	$3 \cdot 10^{-5}$
$\emptyset_{ma}, fraction$	0.08
$\bar{S}_w^{ma}, fraction$	0.4
$VR, fraction$	0
$\mu, kpa \cdot day$	$1.7 \cdot 10^{-11}$
$\bar{K}_w^f, m^2$	$5 \cdot 10^{-13}$
r_e, m	6
$C_A(Rectangular\ shape)$	21.8369
γ	1.781
r_w, m	0.1
$C, kpa \cdot day/m^3$	0.144
$C_{st} \approx \bar{V}_f\bar{\emptyset}_f\bar{C}_t^f\bar{S}_{fw}^f + V_{ma}\emptyset_{ma}C_t^{ma}\bar{S}_w^{ma}, m^3/kpa$	1.58
$m_{RNP} = \frac{B}{C_{st}^{sys}}, kpa/m^3$	0.65 (base case)

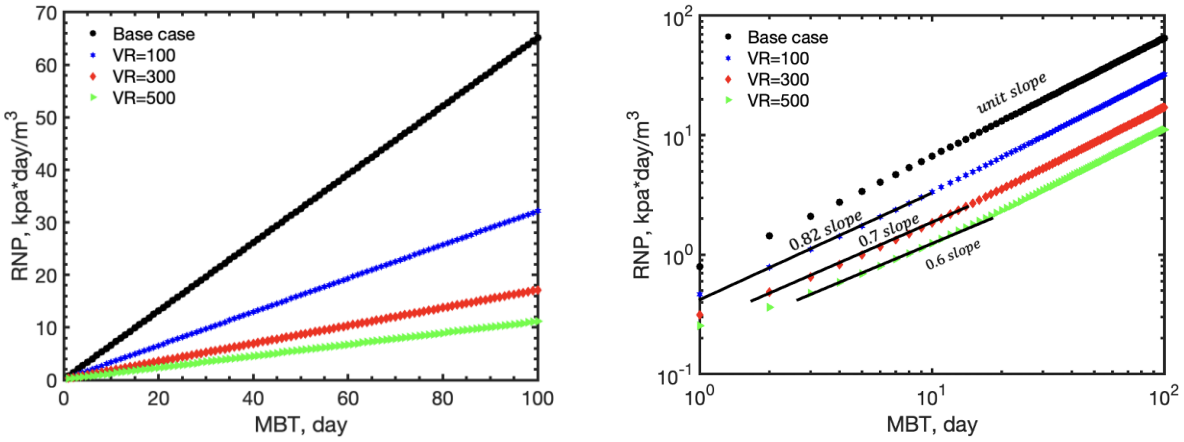

Figure 5.3: Effects of increasing VR on a) cartesian plot, and b) log-log plot of RNP versus MBT.

5.3 Transient state (TS) solution of water RNP diagnostic plot

The extended model in pervious section assumes the whole system under PPS conditions. However, this assumption may not be valid when matrix volume become very large. Therefore, in this section, we assume a transient linear flow of water from matrix into hydraulic fractures during late flowback period.

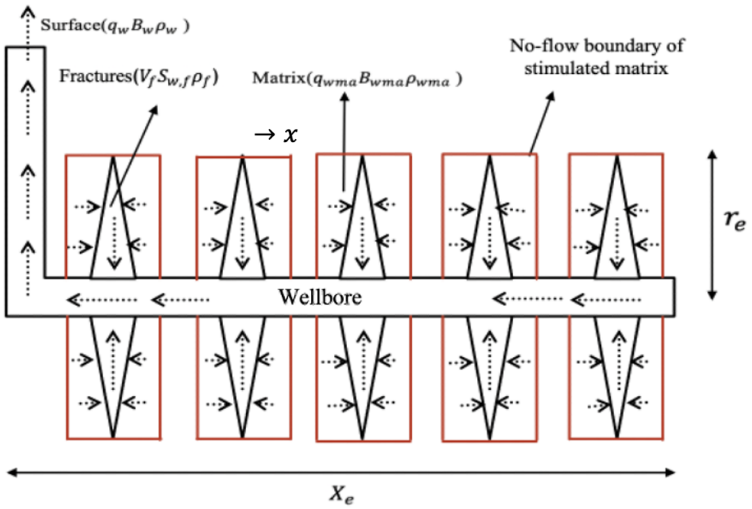

Figure 5.4: 2-D view of a fractured horizontal well in TS model.

The partial differential equation for linear flow of matrix water is given by

$$\frac{\partial^2 P_{ma}}{\partial x^2} = \frac{\bar{\emptyset}_{ma} \bar{C}_t^{ma} \bar{S}_w^{ma} \mu}{\bar{K}_w^{ma}} \frac{\partial P_{ma}}{\partial t} \tag{5.26}$$

Here, x represents the distance away from the fracture-matrix interface along the horizontal direction, as shown in **Figure 5.4**. Next, we define a new dependent variable as

$$p(x,t) = P_i - P_{ma}(x,t) \tag{5.27}$$

Substituting Eq. 5. 27 into Eq. 5. 26 gives

$$\frac{\partial^2 p}{\partial x^2} = \frac{1}{\alpha}\frac{\partial p}{\partial t} \tag{5.28}$$

where, $\alpha = \frac{\bar{K}_w^{ma}}{\emptyset_{ma} C_t^{ma} \bar{S}_w^{ma} \mu}$

We assume constant permeability and total compressibility in the matrix. The initial and boundary conditions are given by

$$p(x,0) = 0 \tag{5.29}$$

$$p(0,t) = P_i - P_f \tag{5.30}$$

$$\lim_{x\to\infty} p(x,t) = 0 \tag{5.31}$$

Here, P_f represents average fracture pressure. Then, we take the Laplace transform of Eq. 5. 28 gives

$$\frac{\partial^2 \bar{p}}{\partial x^2} = -p(x,0) + \frac{s}{\alpha}\bar{p} \tag{5.32}$$

Substituting Eq. 5. 29 into Eq. 5. 32 to arrive at

$$\frac{\partial^2 \bar{p}}{\partial x^2} - \frac{s}{\alpha}\bar{p} = 0 \tag{5.33}$$

Solving Eq. 5. 33 gives

$$\bar{p}(x,s) = Ae^{-x\sqrt{\frac{s}{\alpha}}} + Be^{x\sqrt{\frac{s}{\alpha}}} \tag{5.34}$$

Eq. 5. 31 is valid when $B = 0$, and thus, Eq. 5. 34 becomes

$$\bar{p}(x,s) = Ae^{-x\sqrt{\frac{s}{\alpha}}} \tag{5.35}$$

Next, we take the Laplace transform of Eq. 5. 30 gives

$$\bar{p}(0,s) = \frac{P_i - P_f}{s} \tag{5.36}$$

Substituting Eq. 5. 36 into Eq. 5. 35 gives the solution as

$$\bar{p}(x,s) = \frac{P_i - P_f}{s} e^{-x\sqrt{\frac{s}{\alpha}}} \tag{5.37}$$

For the next step, we take the inverse Laplace transform of Eq. 5. 37 gives

$$\bar{p}(x,s) = (P_i - P_f) erfc(\frac{x}{\sqrt{4\alpha t}}) \tag{5.38}$$

Substituting Eq. 5. 27 into Eq. 5. 38 to arrive the solution as

$$P_{ma}(x,t) = P_i - (P_i - P_f) erfc(\frac{x}{\sqrt{4\alpha t}}) \tag{5.39}$$

q_w^{ma} is given by

$$q_w^{ma} = \frac{\bar{K}_w^{ma} A}{\mu} \frac{\partial P_{ma}}{\partial x}, x = 0 \tag{5.40}$$

Differentiating Eq. 5. 39 with respect to x gives

$$\frac{\partial P_{ma}}{\partial x} = (P_i - P_f) \frac{2}{\sqrt{\pi}} \frac{d}{dx} (\frac{x}{2\sqrt{\alpha t}}) e^{\frac{x^2}{\sqrt{4\alpha t}}} \tag{5.41}$$

When $x = 0$, Eq. 5. 41 gives

$$\frac{\partial P_{ma}}{\partial x} = \frac{1}{\sqrt{\pi}} \frac{P_i - P_f}{\sqrt{\alpha t}} \tag{5.42}$$

For the last step, we substitute Eq. 5. 42 into Eq. 5. 40 gives

$$q_w^{ma} = \frac{A\bar{K}_w^{ma}}{\mu} \frac{1}{\sqrt{\pi}} \frac{P_i - P_f}{\sqrt{\alpha t}} \tag{5.43}$$

Rearranging Eq. 5. 43 gives

$$\frac{P_i - P_f}{q_w^{ma}} = \frac{\mu\sqrt{\pi\alpha}}{\bar{K}_w^{ma} A} \sqrt{t} \tag{5.44}$$

where $\alpha = \frac{\bar{K}_w^{ma}}{\phi_{ma} \bar{S}_w^{ma} \mu C_t^{ma}}$

During the late flowback back period, q_w^{ma} will dominate the water production and the difference between P_{wf} and P_f becomes smaller, and thus, we assume

$$RNP = \frac{P_i - P_{wf}}{q_w^s} \approx \frac{P_i - P_f}{q_w^{ma}} = \frac{\mu\sqrt{\pi\alpha}}{\bar{K}_w^{ma} A}\sqrt{t} \quad (52)$$

Figure 5.5 shows the sensitivity test of m_{RNP} by increasing $\bar{S}_w^{ma}$. We observe that $\bar{S}_w^{ma}$ has no significant effects on the time to observe a half slope on the corresponding log-log plot of RNP versus t. In Abbasi's model, well with negligible water influx will show a unit slope on log-log RNP plot. Therefore, the studied wells with a log-log slope ranges from 0.5 to 1 suggests there is a transition between TS and PSS condition of flowback water.

Table 5.3: Assumed values of each parameter in transient model

System parameters	Assumed values
$C_t^{ma}, 1/kpa$	$3 \cdot 10^{-5}$
$\emptyset_{ma}, fraction$	0.08
$\bar{S}_w^{ma}, fraction$	0.2
$\mu, kpa \cdot day$	$1.7 \cdot 10^{-11}$
$\bar{K}_w^{ma}, m^2$	$5 \cdot 10^{-13}$
r_e, m	6

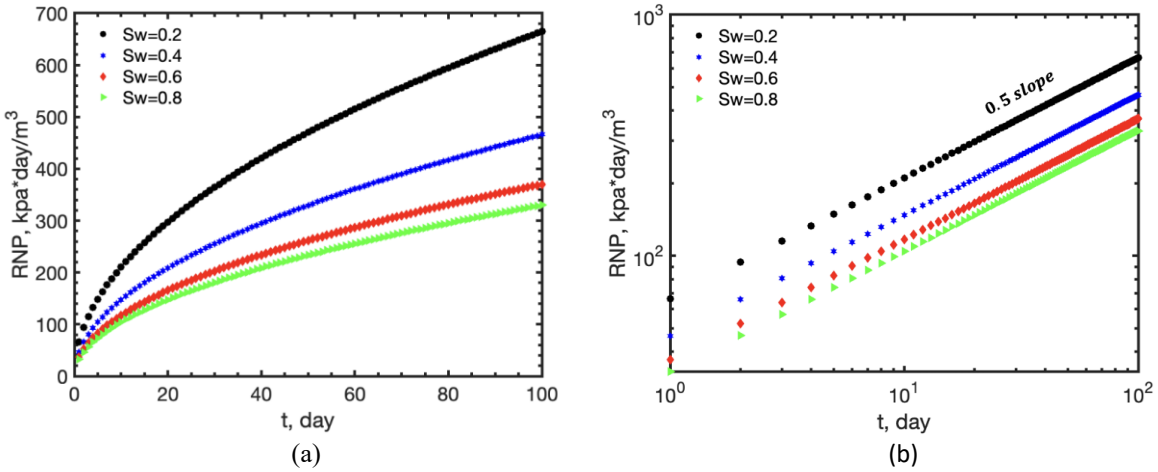

Figure 5.5: Effects of increasing $\bar{S}_w^{ma}$ on a) cartesian plot, and b) log-log plot of RNP versus t.

5.4 Uncertainties and limitations

Here, we discuss the uncertainties and limitations in this study related to the estimation of S_{wi} and our proposed heuristic model.

5.4.1 Heuristic model

1) The proposed PSS models assume the rate of change of pressure with respect to time in the wellbore, the fractures, and the stimulated matrix are almost equal. However, initial fracture permeability is larger than matrix permeability, and thus, the pressure drop with respect to time in the fractures is different from that in the stimulated matrix during early flowback process.

2) The extended mathematical models (PPS and TS models) do not account for secondary fractures. Wells with secondary fractures are expected to have more fluid influx from the matrix system into the fractures.

3) The proposed heuristic model assumes wells with negligible water influx from the matrix start to show a unit slope at very early time of flowback processes (MBT=1 day) on log-log RNP plot. However, the variations of fracture properties may high for wells completed in different formations. Therefore, the time to see a unit slope on log-log RNP plot may change.

4) The proposed heuristic model assumes there is no leak-off of fracturing water. For example, slick-water can easily imbibe into the matrix from the fractures. Therefore, the method may underestimates Q_w^f and overestimates Q_w^{ma}.

5) The proposed method assumes well with negligible water influx show a unit slope on log-log RNP plot. However, for a saturated reservoir, the gas expansion can drag the fracturing fluid flow through hydraulic fractures towards the wellbore. Therefore, the gas expansion increases the water-flowback rate and lead a downward deviation from a unit slope on log-log water RNP plot.

5) The method assumes there is no change in m_{RNP} on log-log RNP plot during the entire flowback process. However, wells with "supercharge effect" show a unit slope at very time of flowback process and start to show a downward deviation from a unit slope after water breakthrough.

5.4.2 Estimation of S_{wi}

1) Log data: Except for the two wells in the first case study, none of the studied wells have log data for their whole horizontal sections. Therefore, we used the log data close to the measured depth of the last fracture stage in the Simandoux equation to estimate an average S_{wi} value.

2) Formation water resistivity: We extracted the values of R_w from the available fluid analysis reports and assigned a mean value at temperatures corresponding to the average measured depth of fracture stages for calculating S_{wi}.

3) Effect of true matrix density on S_{wi}: We used density porosity in sandstone units to measure the porosity of rock matrix for each well at the average measured depth of fracture stages. However, formations may be very heterogenous and the rock types may not be same for all the studied wells. Furthermore, the density porosity is very sensitive to the matrix density. Therefore, the assumed matrix density (ρ_a) may be different from the true matrix density, leading to some errors in

estimated S_{wi}. **Table 5.4** lists major lithologies and lists the possible errors caused by the assumed ρ_a on calculated S_{wi} for wells completed in the Montney, Duvernay and Horn River formations.

Table 5.4: Error analysis of ρ_a for calculating S_{wi} for the Montney, Duvernay, and Horn River wells

	Montney Formation	Duvernay Formation	Horn River Formation
Major lithology and possible matrix density (ρ_p) g/cc	Dark grey shales, 2.4-2.8 Siltstone, 2.73 Sandstone, 2.65	Shales, 2.4-2.8 Limestone, 2.71 Siltstone, 2.4-2.8	Dark silicious shales, 2.4-2.8 Limestone, 2.71
Assumed rock type and ρ_a g/cc	Sandstone, 2.65		
Possible % Error in ρ_a= $\left\|\frac{\rho_a-\rho_p}{\rho_a}\right\| \times 100\%$	0 - 9	0 - 12.9	0 - 12.9
Average bulk density (ρ_b) g/cc	2.55	2.62	2.63
Average porosity ($\emptyset_a$) base on p_b and ρ_a, fraction	0.0601	0.0523	0.0496
Average porosity ($\emptyset_p$) base on p_b and ρ_p, fraction	0.066	0.0351	0.0468
Possible % Error in S_{wi} (Simandoux model)	0 - 5	0 - 18	0 - 4

4) Effect of organic materials on S_{wi}: Linear shale index (I_{sh}) is obtained from the gamma ray log data and was used to estimate V_{sh}. Total gamma ray may overestimate I_{sh} since organic materials may lead to high values of Uranium content. The Duvernay Formation has high organic matter accumulation in transgressive systems tracts and at maximum flooding surfaces (Zhou et al.2021). Similarly, the Horn River Formation has high total organic carbon (TOC) content (Harris et al.2018). In this case, the overestimation of I_{sh} leads to the underestimation of S_{wi}. However, the Montney Formation has less organic matters and the average value of TOC content is around 1.5% from the previous studies (Crombez et al.2015). **Table 5.5** lists the possible measurement errors of I_{sh} on S_{wi} for wells completed in the Duvernay and Horn River formations. In this error analysis,

we assume 1) there are negligible measurement errors in S_{wi} estimation for the Montney wells, 2) the zone with high gamma ray value for the Montney wells gives us the true gamma-ray value of shale (γ_{sh}), and 3) the average gamma ray value of 20 for all the studied wells represents the clean zone with negligible shale contents.

Table 5.5: The calculated error range for calculating S_{wi} for the Duvernay and Horn River formations

	Duvernay wells	Horn River wells
Average gamma ray values of assumed shale layer (γ_a), API	130	136
γ_{sh}, API	105	105
Average % Error in γ_a = $\left\|\frac{\gamma_{sh}-\gamma_a}{\gamma_a}\right\| \times 100\%$	19.2	22.8
Average %Error in I_{sh} = $\left\|\frac{\gamma_a-20}{\gamma_{sh}-20}-1\right\| \times 100\%$	29.4	36.4
Possible %Error in S_{wi} (Simandoux model)	0 - 14.8	0 - 17.6

Chapter 6: Conclusions and Recommendations for Future Study

6.1 Conclusions

We analyzed flowback and log data of 379 oil wells completed in the Montney Formation and 89 oil and gas wells in the Horn River and Duvernay formations of the Western Canadian Sedimentary Basin. We also investigated the effects of water influx from matrix on the slope values of water rate-normalized pressure plots (m_{RNP}) and harmonic decline profiles (m_{HD}). Then, we proposed a heuristic method to approximately estimate matrix and fracturing water contributions to the total produced water during flowback processes. In addition, we extended previous mathematical models by considering water influx from the stimulated matrix into the fractures during flowback processes. Below is the summary of the key results of the study:

• We observe that the semi-log plots of q_w versus Q_w follow harmonic trend during the water-flowback process.

• m_{HD} is inversely correlated to S_{wi} if the studied formations have similar reservoir rock properties such as connate water saturation. This indicates that m_{HD} is inversely correlated to the amount of water influx from matrix into fractures.

• Generally, m_{RNP} is positively correlated to m_{HD} in both case studies. Higher values of m_{RNP} and m_{HD} indicate lower water influx from matrix into fractures.

• Water influx from matrix controls the values of q_w^{ma}, and thus, it controls the deviation from the unit slope on the RNP plots. This can be supported by following observations: 1) wells with lower

m_{HD} show lower m_{RNP} and higher estimated S_{wi}, and 2) the measured Q_w at the end of water-flowback is higher for wells with higher S_{wi} and similar well-completion parameters.

• The applications of our heuristic method on field data shows 1) Q_w^f dominates the total water recovery for wells with higher m_{RNP}, and 2) Q_w^{ma} dominates the total water recovery for wells with lower m_{RNP}.

6.2 Recommendations for Future Study

(1) In this study, we constructed RNP diagnostic plots for oil and gas wells completed in different formations. For gas wells, the gas production will drive the water flow, which will results in lower RNP slope and additional water influx from matrix into fractures. In future study, it is better to distinguish between oil and gas wells. Then, conduct quantitative analysis for oil and gas wells, respectively.

(2) Except for the 2 wells in the first case study, none of the studied wells have log data for their whole horizontal sections. Therefore, we used log data which are close to the measured depth of the first fracture stage in the Simandoux equation to approximately estimate an average S_{wi} value. In future study, it is better to conduct quantitative analysis for wells with available core analysis data, which can give us better estimation of S_{wi}.

(3) We observed that m_{RNP} is proportional m_{HD} and inversely proportional to the amount of formation water influx. Therefore, the results are consistent with our hypothesises. Also, fracturing and formation water contributions can be approximately estimated by our proposed

heuristic model. However, in future study, it is better for us to estimate the actual fracturing and formation water recovery of wells with available water chemical data. Then, compare the actual value with the predict value by using our proposed model.

Bibliography

Abbasi, M., Dehghanpour, H. and Hawkes, R. V. 2012. Flowback Analysis for Fracture Characterization. Presented at the SPE Canadian Unconventional Resources Conference, Calgary, Alberta, Canada, 30 October - 1 November. SPE-162661-MS.

Crafton, J.W., 1998, September. Well evaluation using early time post-stimulation flowback data. In *SPE Annual Technical Conference and Exhibition*. OnePetro.

Clavier C, Coates G, Dumanoir J, 1977. The theoretical and experimental bases for the "dual water" model for the interpretation of shaly sands. In: Society of Petroleum Engineers Paper No. 6859, p 10

Crombez, V., Rohais, S., Baudin, F., Pauthier, S., Riquier, L., Caron, B., ... & Beauvais, L. (2015). Controlling Factors of the Organic Content in the Montney and Doig Formations (Alberta/British Columbia): Insights from Multi-Proxies Analysis and Sequence Stratigraphy.

Coates, G.R., Boutemy, Y. and Clavier, C., 1983. A study of the dual-Water Model Based on Log Data. *Journal of Petroleum Technology*, *35*(01), pp.158-166.

Ezulike, O., Dehghanpour, H., Virues, C., Hawkes, R. V., & Jones Jr, R. S. (2016). Flowback fracture closure: A key factor for estimating effective pore volume. SPE Reservoir Evaluation & Engineering, 19 (04), 567–582.

Ezulike, D.O., Dehghanpour, H. and Hawkes, R.V., 2013, November. Understanding flowback as a transient 2-phase displacement process: An extension of the linear dual-porosity model. In *SPE Unconventional Resources Conference Canada*. OnePetro.

Fu, Yingkun , Dehghanpour, Hassan , Ezulike, Dannel Obinna, and R. Steven Jones. 2017. "Estimating Effective Fracture Pore Volume From Flowback Data and Evaluating Its Relationship to Design Parameters of Multistage-Fracture Completion." *SPE Prod & Oper* 32 : 423–439.

Gdanski, R.D., Weaver, J.D. and Slabaugh, B.F., 2007, January. A new model for matching fracturing fluid flowback composition. In *SPE Hydraulic Fracturing Technology Conference*. OnePetro.

Ghanbari, E., Abbasi, M.A., Dehghanpour, H. and Bearinger, D., 2013, November. Flowback volumetric and chemical analysis for evaluating load recovery and its impact on early-time production. In *SPE Unconventional Resources Conference Canada*. OnePetro.

Hossain, S., Ezulike, O. D., & Dehghanpour, H. (2020). Post-flowback production data suggest oil drainage from a limited stimulated reservoir volume: An Eagle Ford shale-oil case. *International Journal of Coal Geology*, *224*, 103469.

Haolin Zhou, Nicholas B. Harris, Tian Dong, Korhan Ayranci, Jilu Feng, Benoit Rivard, Paul Hackley, Javin Hatcherian, 2021. New insights into organic matter accumulation from high-

resolution geochemical analysis of a black shale: Middle and Upper Devonian Horn River Group, Canada.

Harris, NB, McMillan, JM, Knapp, LJ & Mastalerz, M 2018, 'Organic matter accumulation in the Upper Devonian Duvernay Formation, Western Canada Sedimentary Basin, from sequence stratigraphic analysis and geochemical proxies', *Sedimentary Geology*, vol. 376, pp. 185–203

Ilk, D., Currie, S. M., Symmons, D. et al. 2010. A Comprehensive Workflow for Early Analysis and Interpretation of Flowback Data from Wells in Tight Gas/Shale Reservoir Systems. Presented at SPE Annual Technical Conference and Exhibition, Florence, Italy, 19-22 September. SPE-135607-MS.

Imma Ferrer, E. Michael Thurman, 2015.Chemical constituents and analytical approaches for hydraulic fracturing waters, Trends in Environmental Analytical Chemistry, Volume 5, Pages 18-25, ISSN 2214-1588, https://doi.org/10.1016/j.teac.2015.01.003.

Jones, R. Steven. "Producing Gas-Oil Ratio Behavior of Tight Oil Reservoirs." Paper presented at the SPE/AAPG/SEG Unconventional Resources Technology Conference, San Antonio, Texas, USA, August 2016.

Jones, M.R. and Blasingame, T.A., 2019, July. A direct method for short-term forecasting of multi-phase production rates using flowback data. In *SPE/AAPG/SEG Unconventional Resources Technology Conference*. OnePetro.

J.C.Palacio and T.A.Blasingame, 1993. Decline Curve Analysis Using Type Curves-Analysis of Gas Well Production Data. Paper SPE 25909 presented at Joint Rocky Mountain Regional and Low Permeability Reservoirs Symposium.

Kondash, A.J., Albright, E. and Vengosh, A., 2017. Quantity of flowback and produced waters from unconventional oil and gas exploration. *Science of the Total Environment*, *574*, pp.314-321.

Likhachev, E.R. Dependence of water viscosity on temperature and pressure. *Tech. Phys.* 48**,** 514–515 (2003).

Llera, F.J., Sato, M., Nakatsuka, K. and Yokoyama, H., 1990. Temperature dependence of the electrical resistivity of water-saturated rocks. *Geophysics*, *55*(5), pp.576-585.

Light, T.S., 1984. Temperature dependence and measurement of resistivity of pure water. *Analytical Chemistry*, *56*(7), pp.1138-1142.

Ozkan, E., Raghavan, R. and Apaydin, O.G., 2010, September. Modeling of fluid transfer from shale matrix to fracture network. In *SPE Annual Technical Conference and Exhibition*. OnePetro.

Rashid Olusehun Bello, 2009. Rate Transient Analysis in Shale Gas Reservoirs with Transient Linear Behavior.

Sabbir Hossain, Obinna D. Ezulike, and Hassan Dehghanpour. 2019. Estimating Residual Fracture Pore Volume by Analyzing Post-Flowback Water Production: An Eagle Ford Black-Oil Case. URTeC: 2019-A-989

Tamer Moussa, Fu, Yingkun , Dehghanpour, Hassan , and Robert Hawkes. 2020. "Coupled Versus Stratified Flow of Water and Hydrocarbon During Flowback and Post-flowback Processes."

Tamer Moussa, Hassan Dehghanpour, Yingkun Fu, and Obinna Ezulike. 2019. Dynamic Fracture Volume Estimation using Flowback Data Analysis and its Correlation to Completion-Design Parameters. SPE-194322-MS

Yang, R., Huang, Z., Li, G., Yu, W., Sepehrnoori, K., Tian, S., Song, X. and Sheng, M., 2016, September. An innovative approach to model two-phase flowback of shale gas wells with complex fracture networks. In *SPE Annual Technical Conference and Exhibition*. OnePetro.

Vaisblat, N., Harris, N.B., DeBhur, C., Euzen, T., Gasparrini, M., Crombez, V., Rohais, S., Krause, F. and Ayranci, K. (2017): Diagenetic model for the deep Montney Formation, northeastern British Columbia; *in* Geoscience BC Summary of Activities 2016, Geoscience BC, Report 2017-1, p. 37–48.

Vaisblat, N., 2020. Controls on Reservoir Quality in the Lower Triassic Montney Formation, Chapter 5.

Williams-Kovacs, J.D. and Clarkson, C.R., 2013, November. Stochastic modeling of multi-phase flowback from multi-fractured horizontal tight oil wells. In *SPE Unconventional Resources Conference Canada*. OnePetro.

Wattenbarger, R.A., El-Banbi, A.H., Villegas, M.E. and Maggard, J.B., 1998, April. Production analysis of linear flow into fractured tight gas wells. In *SPE rocky mountain regional/low-permeability reservoirs symposium*. OnePetro.

Warner, N.R., Darrah, T.H., Jackson, R.B., Millot, R., Kloppmann, W. and Vengosh, A., 2014. New tracers identify hydraulic fracturing fluids and accidental releases from oil and gas operations. *Environmental science & technology*, *48*(21), pp.12552-12560.

Weides, Simon & Majorowicz, Jacek. (2014). Implications of Spatial Variability in Heat Flow for Geothermal Resource Evaluation in Large Foreland Basins: The Case of the Western Canada Sedimentary Basin. Energies. 2014. 2573-2594. 10.3390/en7042573.

Xu, Y., Adefidipe, O. and Dehghanpour, H., 2016. A flowing material balance equation for two-phase flowback analysis. *Journal of Petroleum Science and Engineering*, *142*, pp.170-185.

Yingkun Fu, Hassan Dehghanpour. 2019. Advances in Flowback Analysis: Fracturing Water Production Obeys a Simple Decline Model, Chapter 1.

Zolfaghari, A., Holyk, J., Tang, Y., Dehghanpour, H. and Bearinger, D., 2015. Flowback chemical analysis: An interplay of shale-water interactions. In *SPE Asia Pacific Unconventional Resources Conference and Exhibition*. Society of Petroleum Engineers.

Zolfaghari, A., Dehghanpour, H., Ghanbari, E.et al. . 2016. Fracture Characterization Using Flowback Salt-Concentration Transient. *SPE J*. 21 (1): 233–244. SPE-168598-PA.

Zhang, F. and Emami-Meybodi, H., 2020. Multiphase flowback rate-transient analysis of shale gas reservoirs. *International Journal of Coal Geology*, *217*, p.103315.

Appendix A

Figure A-1 shows partial measured depth versus gamma ray log data for a sample oil well. The linear shale index is used as an approximate value of *Vsh* in the Simandoux equation. In this case, the section which shows the gamma-ray value of 120 represents the shale layer, and the section which shows the gamma-ray value of 55 represents a relatively clean zone with negligible shale content.

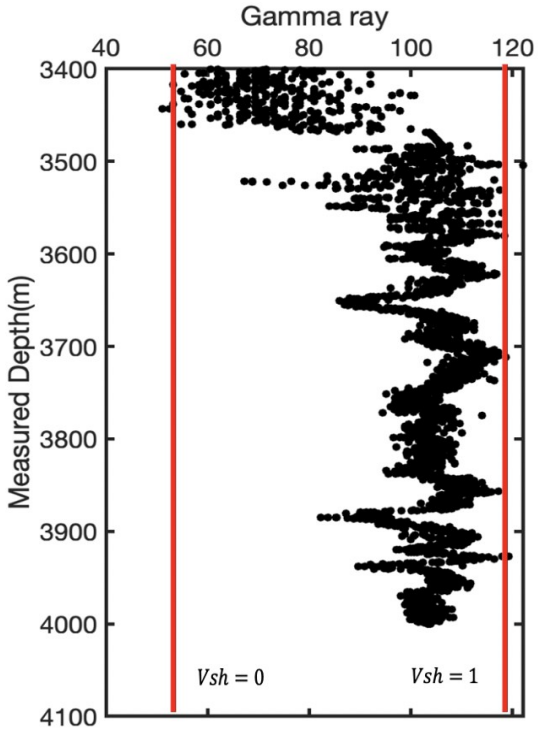

Figure A-1: Measured depth versus Gamma ray for sample oil well. Linear shale index is used as the value of *Vsh* in the Simandoux equation

Appendix B

This section presents the results of 3 sample applications of our heuristic method. The results show that Q_w^f dominates the total water recovery for wells with higher m_{RNP}, and Q_w^{ma} dominates the total water recovery for wells with lower m_{RNP}.

Well A

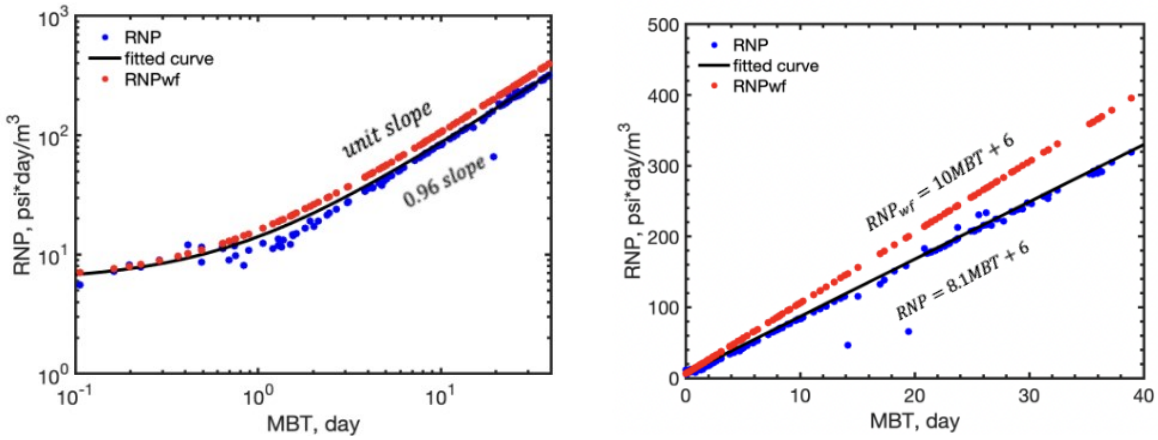

(a) (b)

Figure B-1: RNP versus MBT for sample oil well A on a) log-log plot and b) cartesian plots

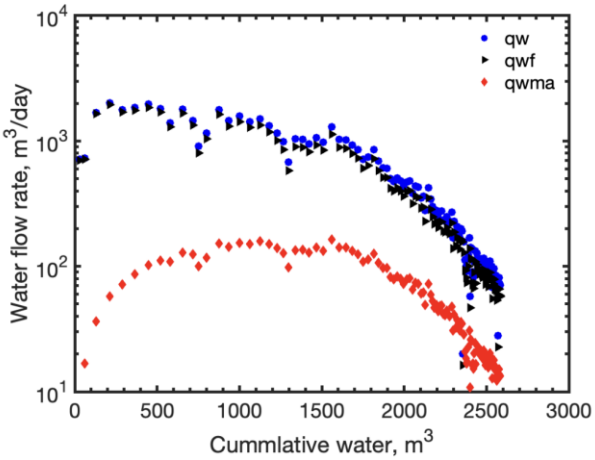

Figure B-2: Semi-log plots of q_w, q_w^f, and q_w^{ma} versus Q_w for a sample oil well A

Table B-1: Calculated values for Q_w^{ma} and Q_w^f at the end of the flowback process for the sample oil well A

Q_w m^3	AAPE, fraction	Q_w^f m^3	Q_w^{ma} m^3	TIV m^3	Q_w/TIV fraction	Q_w^f/TIV fraction	Q_w^{ma}/TIV fraction
2600	0.032	2120 ± 67.8	480 ± 15.4	8294	0.31 ± 0.01	0.26 ± 0.008	0.05 ± 0.002

Well B

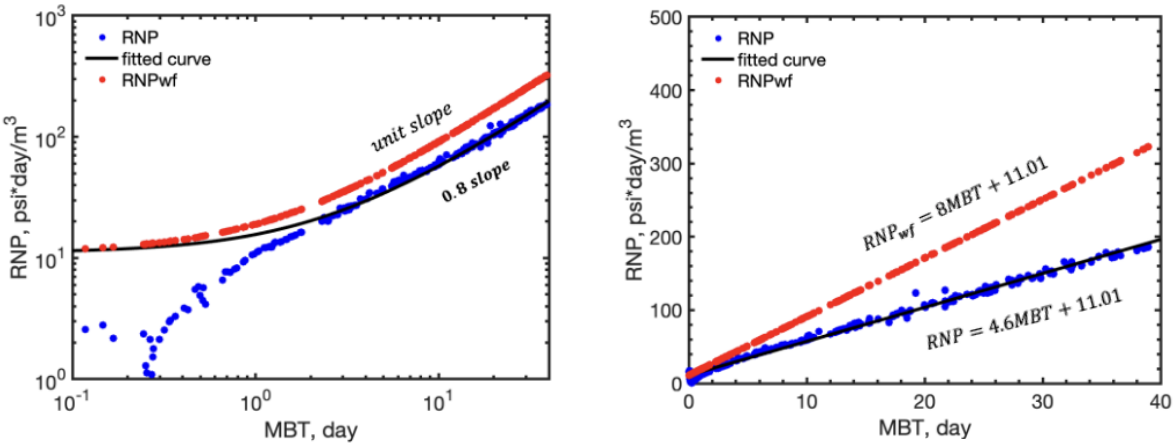

(a) (b)

Figure B-3: RNP versus MBT for sample oil well B on a) log-log plot and b) cartesian plots

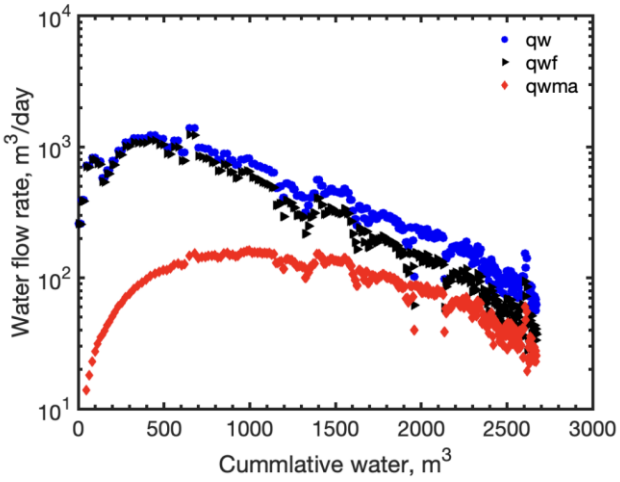

Figure B-4: Semi-log plots of q_w, q_w^f, and q_w^{ma} versus Q_w for a sample oil well B

Table B-2: Calculated values for Q_w^{ma} and Q_w^f at the end of the flowback process for the sample oil well B

Q_w m^3	AAPE, fraction	Q_w^f m^3	Q_w^{ma} m^3	TIV m^3	Q_w/TIV fraction	Q_w^f/TIV fraction	Q_w^{ma}/TIV fraction
2650	0.028	1650 ± 46.2	1000 ± 28	7221	0.37 ± 0.01	0.23 ± 0.006	0.14 ± 0.004

Well C

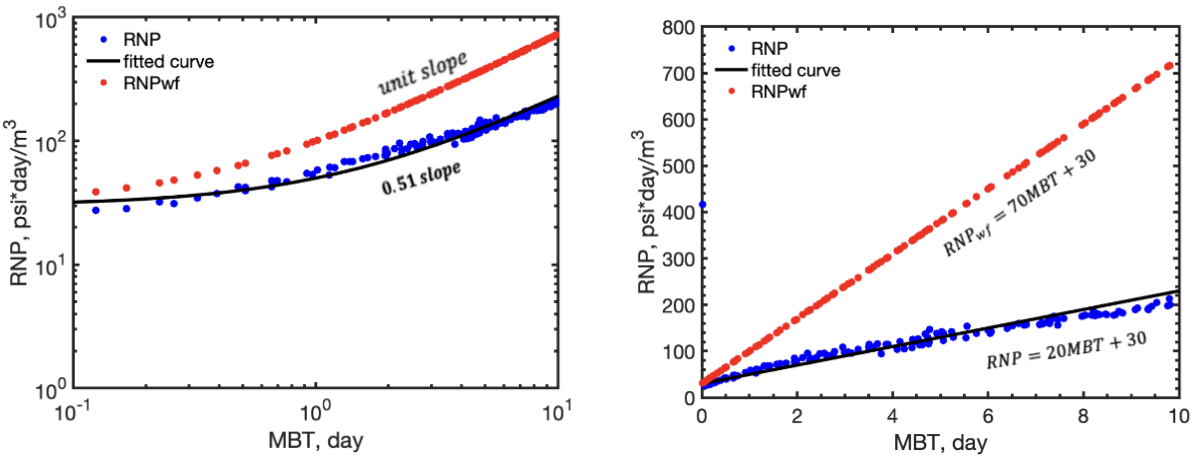

(a) (b)

Figure B-5: RNP versus MBT for sample oil well C on a) log-log plot and b) cartesian plots

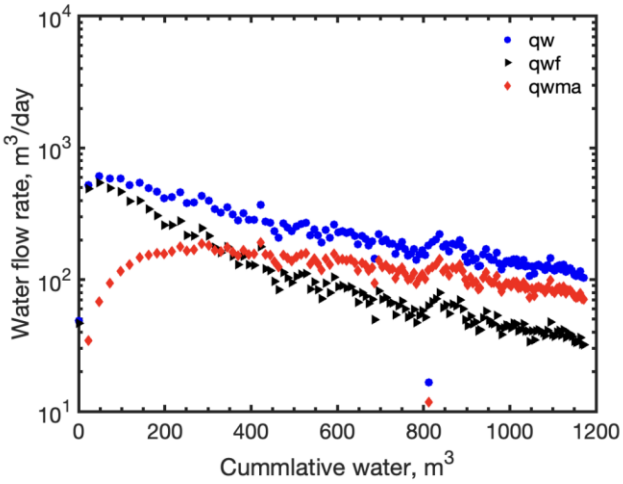

Figure B-6: Semi-log plots of q_w, q_w^f, and q_w^{ma} versus Q_w for a sample oil well C

Table B-3: Calculated values for Q_w^{ma} and Q_w^f at the end of the flowback process for the sample oil well C

Q_w m^3	AAPE, fraction	Q_w^f m^3	Q_w^{ma} m^3	TIV m^3	Q_w/TIV fraction	Q_w^f/TIV fraction	Q_w^{ma}/TIV fraction
1200	0.071	300 ± 21.3	900 ± 63.9	3994	0.3 ± 0.02	0.075 ± 0.005	0.225 ± 0.015